



# Calculation of predictions for non-identical particle correlations in heavy ions collisions at LHC energies from hydrodynamics-inspired models

MASTER OF SCIENCE THESIS

Author:  
**Mateusz Wojciech Gałażyn**

Supervisor:  
**Prof. Adam Kisiel**

Warsaw, 15th December 2014



# Wyznaczenie przewidywań teoretycznych dla korelacji cząstek nieidentycznych w zderzeniach ciężkich jonów przy energiach LHC w modelach opartych na hydrodynamice

PRACA MAGISTERSKA

Autor:  
**Mateusz Wojciech Gałażyn**

Promotor:  
**dr hab. inż. Adam Kisiel, prof. PW**

Warszawa, 15 grudnia 2014

## Abstract

This thesis presents results of two-particle momentum correlations analysis for selected types of particles produced in heavy ion collisions. The studies were carried for the data from lead-lead collisions at the centre of mass energy  $\sqrt{s_{NN}} = 2.76$  TeV simulated in the THERMINATOR model using the (3+1)-dimensional hydrodynamic model with viscosity. Analysis was performed for the three particle types: pions, kaons and protons for the collisions in eight centrality ranges.

The THERMINATOR model allows to perform statistical hadronization of stable particles and unstable resonances from a given hypersurface. It is followed by the resonance propagation and decay phase. The four-dimensional hypersurface is taken from the calculations performed in relativistic hydrodynamic framework with the viscosity corrections.

One can investigate space-time characteristics of the particle-emitting source through two-particle interferometry. The experimental-like analysis of the data coming from a model calculations yields the possibility to test the hydrodynamic description of a quark-gluon plasma. This thesis concentrates on the verification of the prediction of the appearance of scaling of femtoscopic radii with transverse mass.

The three dimensional correlation functions were calculated using spherical harmonics decomposition. One can use this approach to perform calculations with lower statistics and moreover the visualization of results is much easier. The calculated correlation functions show expected increase of a correlation for pions and kaons at the low relative momenta of a pair. For the protons at the same momentum region, the decrease occurs. Furthermore, the transverse pair momentum and centrality dependence on a correlation function is observed. In order to perform the quantitative analysis of this influence, the fitting of theoretical formula for correlation function was performed. The femtoscopic radii calculated in the Longitudinally Co-Moving System and Pair Rest Frame are falling with the transverse mass  $m_T$ . To test the scaling predicted from the hydrodynamics, the power-law  $\alpha m_T^{-\beta}$  was fitted. The radii calculated for pions, kaons and protons in the LCMS are following the common scaling. In the case of the PRF such scaling is not observed. To recover the scaling in the PRF, the approximate factor is proposed:  $\sqrt{(\sqrt{\gamma_T} + 2)/3}$ . The radii in the PRF divided by the proposed scaling factor are falling on the common curve, proving that the scaling can be recovered using the proposed factor. The experimental analysis is usually performed in the PRF (requires less statistics), hence the method of scaling recovery enables easier testing of the hydrodynamic predictions, also in the PRF.

## Streszczenie

W tej pracy zaprezentowane są wyniki analizy dwucząstkowych korelacji pędowych dla trzech wybranych typów cząstek produkowanych w zderzeniach ciężkich jonów. Obliczenia zostały wykonane dla danych ze zderzeń ołów-ołów przy energii w centrum masy  $\sqrt{s_{NN}} = 2.76 \text{ TeV}$  wygenerowanych za pomocą modelu THERMINATOR przy użyciu (3+1)-wymiarowego modelu hydrodynamicznego uwzględniającego lepkość ośrodka. Analiza została wykonana dla pionów, kaonów i protonów dla dziewięciu przedziałów centralności.

Model THERMINATOR wykonuje statystyczną hadronizację stabilnych cząstek jak i również niestabilnych rezonansów z danej hiperpowierzchni wymrażania, a następnie uwzględnienia propagację i rozpad tych rezonansów. Czterowymiarowa hiperpowierzchnia pochodzi z obliczeń przeprowadzonych na podstawie hydrodynamiki relatywistycznej z uwzględnieniem poprawek pochodzących od lepkości.

Interferometria dwucząstkowa pozwala na zbadanie charakterystyk czasowo-przestrzennych źródła cząstek. Poprzez analizę danych pochodzących z obliczeń modelowych można dokonać sprawdzenia zakresu stosownalności hydrodynamiki do opisu właściwości plazmy kwarkowo-gluonowej. Ta praca koncentruje się na weryfikacji skalowania promieni femtoskopowych z masą poprzeczną przewidywanego przez hydrodynamikę.

Wyliczone trójwymiarowe funkcje korelacyjne zostały rozłożone w szereg harmonik sferycznych. To podejście wymaga mniejszej statystyki i pozwala na łatwiejszą wizualizację wyników. Wyliczone funkcje wykazują oczekiwany wzrost korelacji dla niskich różnic pędów dla par pionów i kaonów. Z kolei dla par protonów w tym samym zakresie pędów można zauważać wyraźny spadek korelacji. Przy tym, we wszystkich przypadkach zderzeń jest widoczny wpływ pędu poprzecznego pary oraz centralności na funkcję korelacyjną. W celu wykonania analizy ilościowej tego wpływu, zostało wykonane dopasowanie formuły analitycznej do obliczonych funkcji korelacyjnych. Otrzymane w ten sposób promienie femtoskopowe w LCMS i PRF wykazują spadek wraz z wzrostem masy poprzecznej  $m_T$ . W celu sprawdzenie skalowania przewidywanego przez hydrodynamikę została dopasowana zależność potęgowa:  $\alpha m_T^{-\beta}$ . Promienie obliczone dla pionów, kaonów i protonów zachowują wzajemne skalowanie w LCMS. W przypadku PRF skalowanie nie jest widoczne, więc aby je odzyskać został zaproponowany przybliżony współczynnik skalowania w postaci:  $\sqrt{(\sqrt{\gamma_T} + 2)/3}$ . Promienie w PRF po podzieleniu przez tą wartość, dają się opisać oczekowaną zależnością potęgową.

Analiza eksperymentalna jest zazwyczaj wykonywana w PRF, bowiem wymaga w tym układzie odniesienia mniejszej statystyki. Zatem metoda odzyskania skalowania pozwala na łatwiejszą, w porównaniu z LCMS, weryfikację przewidywań hydrodynamiki, które nie są widoczne w PRF.

# Contents

<b>Introduction</b>	<b>1</b>
<b>1 Theory of heavy ion collisions</b>	<b>3</b>
1.1 The Standard Model . . . . .	3
1.2 Quantum Chromodynamics . . . . .	4
1.2.1 Quarks and gluons . . . . .	4
1.2.2 Quantum Chromodynamics potential . . . . .	5
1.2.3 The quark-gluon plasma . . . . .	7
1.3 Relativistic heavy ion collisions . . . . .	9
1.3.1 Stages of heavy ion collision . . . . .	9
1.3.2 QGP signatures . . . . .	11
<b>2 Therminator model</b>	<b>19</b>
2.1 (3+1)-dimensional viscous hydrodynamics . . . . .	19
2.2 Statistical hadronization . . . . .	20
2.2.1 Cooper-Frye formalism . . . . .	21
2.3 Event generation procedure . . . . .	22
<b>3 Particle interferometry</b>	<b>25</b>
3.1 The HBT interferometry . . . . .	25
3.2 Theoretical approach . . . . .	25
3.2.1 Conventions used . . . . .	26
3.2.2 Two particle wave function . . . . .	27
3.2.3 Source emission function . . . . .	28
3.2.4 Analytical form of a correlation function . . . . .	31
3.2.5 Spherical harmonics decomposition of a correlation function	31
3.3 Experimental approach . . . . .	33
3.4 Scaling of femtoscopic radii . . . . .	33
3.4.1 Scaling in LCMS . . . . .	34
3.4.2 Scaling in PRF . . . . .	35
<b>4 Results</b>	<b>36</b>
4.1 Identical particles correlations . . . . .	36
4.1.1 Spherical harmonics components . . . . .	36

4.1.2	Centrality dependence of a correlation function . . . . .	40
4.1.3	$k_T$ dependence of a correlation function . . . . .	41
4.2	Results of the fitting procedure . . . . .	42
4.2.1	The three-dimensional femtoscopic radii scaling . . . . .	42
4.2.2	Scaling of one-dimensional radii . . . . .	47
4.3	Discussion of the results . . . . .	48
<b>Conclusions</b>		<b>49</b>
<b>A Correlation function calculation scripts</b>		<b>51</b>
A.1	Events generation . . . . .	51
A.2	Calculations of experimental-like correlation functions . . . . .	52
<b>B Fitting utilities</b>		<b>53</b>
B.1	Minuit package . . . . .	53
B.2	Fitting software . . . . .	53
B.2.1	Input parameters . . . . .	53
B.2.2	Output format . . . . .	55
B.2.3	Compilation . . . . .	55
B.2.4	Usage . . . . .	55
<b>C Plotting scripts</b>		<b>57</b>
C.1	Correlation functions plots . . . . .	57
C.2	Plots with femtoscopic radii . . . . .	57

# Introduction

Many people were trying to discover what was in the beginning of the Universe which we observe today. Through the years, many theories were formulated to describe its origin and behaviour. Among them is one model, which provides a comprehensive explanation for a broad range of phenomena, including the cosmic microwave background, abundance of the light elements and Hubble's law. This model is called The Big Bang theory and has been born in 1927 on the basis of the principles proposed by the Belgian priest and scientist Georges Lemaître. Using this model and known laws of physics one can calculate the characteristics of the Universe back in time to the extreme densities and temperatures. However, at some point these calculations fail. The extrapolation of the expansion of the Universe backwards in time using general relativity yields an infinite density and temperature at a finite time in the past. This appearance of singularity is a signal of the breakdown of general relativity. The range of this extrapolation towards singularity is debated - certainly we can go no closer than the end of the *Planck epoch* i.e.  $10^{-43}$  s. At this very first era the temperature of the Universe was so high, that the four fundamental forces: electromagnetism, gravitation, weak nuclear interaction and strong nuclear interaction were one fundamental force. Between  $10^{-43}$  s and  $10^{-36}$  s of a lifetime of the Universe, there is a *grand unification epoch*, at which forces are starting to separate from each other. The *electroweak epoch* lasted from  $10^{-36}$  s to  $10^{-12}$  s, when the strong force separated from the electroweak force. After this epoch, there was the *quark epoch* in which the Universe was a dense "soup" of quarks. During this stage the fundamental forces of gravitation, electromagnetism, strong and weak interactions had taken their present forms. The temperature at this moment was still too high to allow quarks to bind together and form hadrons. At the end of quark era, there was a big freeze-out - when the average energy of particle interactions had fallen below the binding energy of hadrons. This era, in which quarks became confined into hadrons, is known as the *hadron epoch*. At this moment the matter had started forming nuclei and atoms, which we observe today.

Here arises the question: how can we study the very beginning of the Universe? To do this, one should recreate in a laboratory appropriate conditions i.e. such large density and high temperature. Today, this is achievable through sophisticated machines like particle accelerators. Sufficiently high energies are available at the Large Hadron Collider at CERN, Geneva and Relativistic Heavy Ion

Collider at Brookhaven National Laboratory in Upton, New York. In the particle accelerators the heavy ions after being accelerated to near the speed of light are collided in order to generate extremely dense and hot phase of matter and re-create the quark-gluon plasma. The plasma is believed to behave like an almost ideal fluid, which can be described by the laws of relativistic hydrodynamics.

This thesis is providing predictions for collective behaviour of the quark-gluon plasma coming from the hydrodynamic equations. Experimental-like analysis was performed for the high energy Pb-Pb collisions generated with the THERMINATOR model.

The 1st chapter is an introduction to the theory of heavy ion collisions. It contains the brief description of the Standard Model and Quantum Chromodynamics. Moreover the quark-gluon plasma and its signatures are also characterized.

In the 2nd chapter, the relativistic hydrodynamic framework and the THERMINATOR model used to perform the simulations of collisions are described.

The 3rd chapter covers the particle interferometry method used in this work. Predictions coming from the hydrodynamics are also presented here. An algorithm of building experimental correlation functions is described as well.

In the 4th chapter, an interpretation of the results for two-particle femtoscopy for different pairs of particles is presented. Moreover, the quantitative analysis of the calculated femtoscopic radii as well as the appearance of transverse mass scaling is discussed.

In the Appendices, the detailed description of the tools developed by the author and used in this work is given. Utilities for managing the event generation process and plotting of correlation functions are presented. Furthermore, the fitting software, its design and usage is described.

# Chapter 1

## Theory of heavy ion collisions

### 1.1 The Standard Model

In the 1970s, a new theory of fundamental particles and their interactions emerged. It was a new concept, which combined the electromagnetic, weak and strong nuclear interactions between known particles. This theory is called *The Standard Model*. There are seventeen named particles in the standard model, organized into the chart shown below (Fig. 1.1). Fundamental particles are divided into two families: *fermions* and *bosons*.

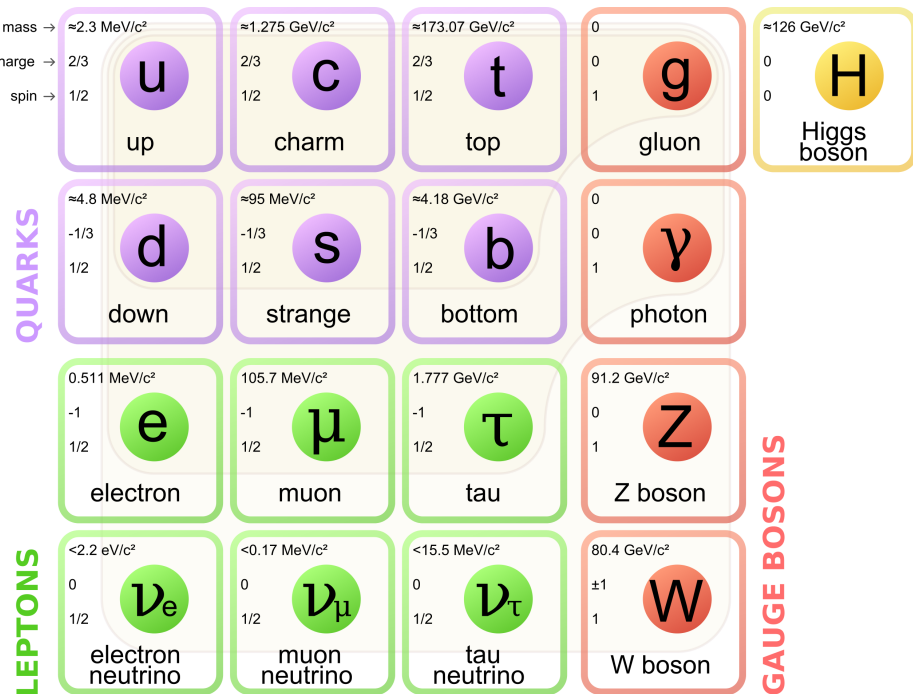


Figure 1.1: The Standard Model of elementary particles [1].

Fermions are the building blocks of matter. They are divided into two groups. Six of them, which must bind together are called *quarks*. Quarks are known to bind into doublets (*mesons*), triplets (*baryons*) and recently confirmed four-quark states<sup>1</sup>. Two of baryons, with the longest lifetimes, are forming a nucleus: a proton and a neutron. A proton is build from two up quarks and one down, and neutron consists of two down quarks and one up. The first one is found to be a stable particle (at least it has a lifetime larger than  $10^{35}$  years) while a free neutron has a mean lifetime about  $8.8 \times 10^2$  s. Fermions that can exist independently are called *leptons*. Neutrinos are a subgroup of leptons, which are only influenced by the weak interaction. In principle, fermions can be divided into three generations (three columns in the Figure 1.1). Quarks from the first generation can combine into hadrons with the longest life spans. Generation II and III consists of unstable quarks which also form unstable hadrons.

In turn, bosons are force carriers. There are four fundamental forces: weak - responsible for radioactive decay, strong - coupling quarks into hadrons, electromagnetic - between charged particles and gravity - the weakest, which causes the attraction between particles with mass. The Standard Model describes the first three. The weak force is mediated by  $W^\pm$  and  $Z^0$  bosons, electromagnetic force is carried by photons  $\gamma$  and the carriers of a strong interaction are gluons  $g$ . Finally, the fifth boson is a Higgs boson which is responsible for giving other particles mass.

## 1.2 Quantum Chromodynamics

### 1.2.1 Quarks and gluons

Quarks interact with each other through the strong interaction. The mediator of this force is a *gluon* - a massless and electrical chargeless particle. In the quantum chromodynamics (QCD) - theory describing strong interaction - there are six types of "charges" (like electrical charges in the electrodynamics) called *colours*. The colours were introduced because some of the observed particles, like  $\Delta^-$ ,  $\Delta^{++}$  and  $\Omega^-$  appeared to consist of three quarks with the same flavour ( $ddd$ ,  $uuu$  and  $sss$  respectively), which was in conflict with the Pauli exclusion principle. One quark can carry one of the three colours (usually called *red*, *green* and *blue*) while an antiquark one of the three anti-colours respectively. Only colour-neutral (or white) particles could exist. Mesons are assumed to be a colour-anticolour pair, while baryons are *red-green-blue* triplets. Gluons also are colour-charged and there are 8 types of gluons. Therefore they can interact with themselves [3].

---

<sup>1</sup>The LHCb experiment at CERN in Geneva confirmed recently the existence of  $Z(4430)$  - a particle consisting of four quarks [2].

### 1.2.2 Quantum Chromodynamics potential

As a result of the fact that gluons are massless, one can expect, that the static potential in QCD will have the form similar to the one in electrodynamics e.g.  $\sim 1/r$  (by analogy to photons). In reality the QCD potential is assumed to have the form of [3]:

$$V_s = -\frac{4}{3} \frac{\alpha_s}{r} + kr, \quad (1.1)$$

where the  $\alpha_s$  is a coupling constant of the strong force and the  $kr$  part is related with *confinement*. In comparison to the electromagnetic force, a value of the strong coupling constant is  $\alpha_s \approx 1$  and the electromagnetic one is  $\alpha = 1/137$ .

The fact that quarks does not exist separately and are always bound, is called confinement. As two quarks are pulled apart, the linear part  $kr$  in the Eq. 1.1 becomes dominant and the potential becomes proportional to the distance. This situation resembles stretching of a string. At some point, when the string is so large it is energetically favourable to create a quark-antiquark pair. After formation of such pair (or pairs), the string breaks and the confinement is preserved (Fig. 1.2).

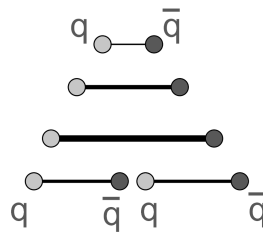


Figure 1.2: A string breaking and a creation of a new quark-anti-quark pair [4].

On the other hand, for small  $r$ , an interaction between the quarks and gluons is dominated by the Coulomb-like term  $-\frac{4}{3} \frac{\alpha_s}{r}$ . The coupling constant  $\alpha_s$  depends on the four-momentum  $Q^2$  transferred in the interaction. This dependence is presented in Fig. 1.3. The value  $\alpha_s$  decreases with increasing momentum transfer and the interaction becomes weak for large  $Q^2$ , i.e.  $\alpha_s(Q) \rightarrow 0$ . Because of the weakening coupling constant, quarks at large energies (or small distances) are starting to behave like free particles. This phenomenon is known as *asymptotic freedom*. The QCD potential also exhibits a temperature dependence - the force strength “melts” with the temperature increase. Therefore the asymptotic freedom is expected to appear in either the case of high baryon densities (small distances between quarks) or very high temperatures. This temperature dependence is illustrated in Fig. 1.4.

If the coupling constant  $\alpha_s$  is small, one can use perturbative methods to calculate physical observables. Perturbative QCD (pQCD) successfully describes hard processes (with large  $Q^2$ ) such as jet production in high energy proton-antiproton collisions. The applicability of pQCD is defined by the *scale parameter*  $\Lambda_{QCD} \approx 200$  MeV. If  $Q \gg \Lambda_{QCD}$  then the process is in the perturbative



Figure 1.3: The coupling parameter  $\alpha_s$  dependence on four-momentum transfer  $Q^2$  [5].

domain and can be described by pQCD. A description of soft processes (when  $Q < 1$  GeV) is a problem in QCD - perturbative theory breaks down at this scale. Therefore, to describe reactions with low  $Q^2$ , one has to use alternative methods like Lattice QCD. Lattice QCD (LQCD) is non-perturbative implementation of a field theory in which QCD quantities are calculated on a discrete space-time grid. LQCD allows to obtain properties of matter in equilibrium, but there are some limitations. First of all, Lattice QCD requires fine lattice spacing to obtain precise results. Therefore large computational resources are necessary. However, nowadays with the constant growth of computing power this problem will become less important. The second problem is that lattice simulations are possible only for baryon density  $\mu_B = 0$ . At  $\mu_B \neq 0$ , Lattice QCD breaks down because of the sign problem. In QCD the thermodynamic observables are related to the grand canonical partition function, which has a baryonic chemical potential  $\mu_B$  as a parameter. Therefore, the baryonic density can be controlled by tuning the baryonic chemical potential. For fermions  $\mu_B$  can be both positive and negative. For particles with  $\mu_B$ , their antiparticles have chemical potentials with opposite sign  $-\mu_B$ . Since in the early universe the number of baryons and antibaryons were almost equal we can use  $\mu_B = 0$  to a very good approximation [6].

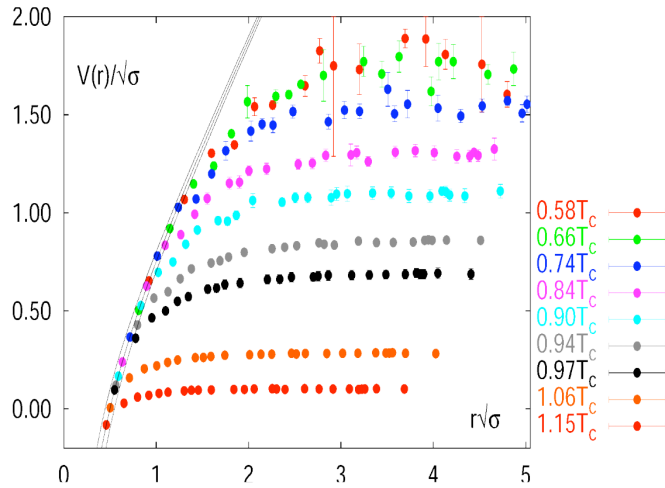


Figure 1.4: The QCD potential for a quark-antiquark pair as a function of distance for different temperatures. A value of the potential decreases with the temperature [4].

### 1.2.3 The quark-gluon plasma

The new state of matter in which quarks are no longer confined is known as a *quark-gluon plasma* (QGP). The predictions coming from the discrete space-time Lattice QCD calculations reveal a phase transition from the hadronic matter to the quark-gluon plasma at the high temperatures and baryon densities. The results obtained from these calculations are shown on Fig. 1.5. The energy density  $\epsilon$  which is divided by  $T^4$  is a measure of the number of degrees of freedom in the

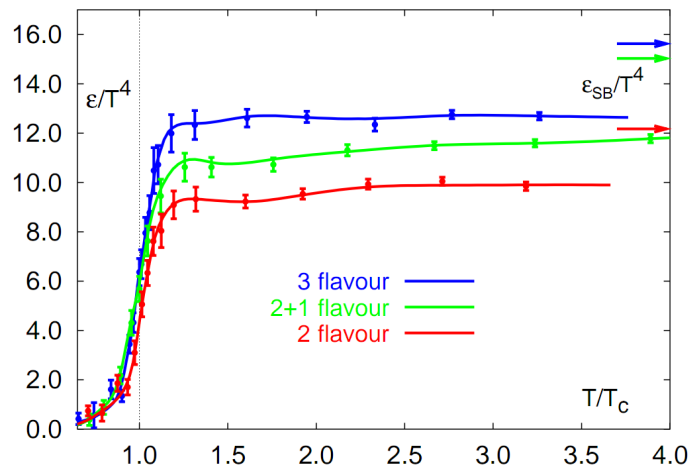


Figure 1.5: A number of degrees of freedom as a function of a temperature [7].

system. One can observe significant growth of this value, when the temperature rises past the critical value  $T_C$ . Such increase is signaling a phase transition - the formation of QGP [8]. The values of the energy densities plotted in Fig. 1.5 do not reach the Stefan-Boltzmann limit  $\epsilon_{SB}$  (marked with arrows), which corresponds to an ideal gas. This can indicate some residual interactions in the system. According to the results from the RHIC<sup>2</sup>, the new phase of matter behaves more like an ideal fluid, than like a gas [9].

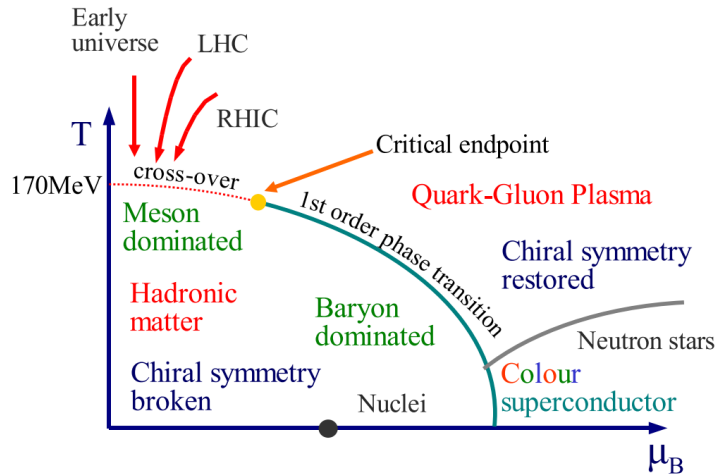


Figure 1.6: Phase diagram coming from the Lattice QCD calculations [8].

One of the key questions, to which current heavy ion physics tries to find an answer is the value of a critical temperature  $T_C$  as a function of a baryon chemical potential  $\mu_B$  (baryon density), where the phase transition occurs. The results coming from the Lattice QCD are presented in Fig. 1.6. The phase of matter in which quarks and gluons are deconfined is expected to exist at large temperatures. On the other side, in the region of small temperatures and high baryon densities, a different state is supposed to appear - a *colour superconductor*. The phase transition between hadronic matter and the QGP is thought to be of 1<sup>st</sup> order at  $\mu_B \gg 0$ . However as  $\mu_B \rightarrow 0$  quarks' masses become significant and a sharp transition transforms into a rapid but smooth cross-over. It is believed that in Pb-Pb collisions observed at the LHC<sup>3</sup>, the created matter has temperature high enough to be in the quark-gluon plasma phase, then cools down and converts into hadrons, undergoing a smooth transition [8].

<sup>2</sup>Relativistic Heavy Ion Collider at Brookhaven National Laboratory in Upton, New York

<sup>3</sup>Large Hadron Collider at CERN, Geneva

## 1.3 Relativistic heavy ion collisions

### 1.3.1 Stages of heavy ion collision

To create the quark-gluon plasma one has to achieve sufficiently high temperatures and baryon densities. Such conditions can be recreated in the heavy ion collisions at the high energies. The left side of the Figure 1.7 shows simpli-

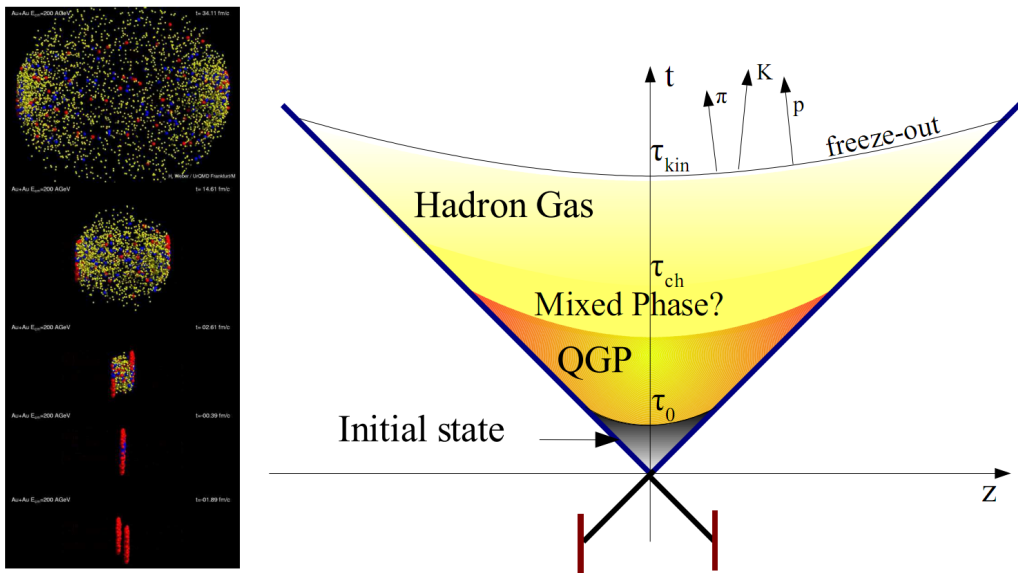


Figure 1.7: Left: stages of a heavy ion collision simulated in the UrQMD model. Right: schematic view of a heavy ion collision evolution [8].

fied picture of a central collision of two highly relativistic nuclei in the centre-of-mass reference frame. The colliding nuclei are presented as thin disks because of the Lorentz contraction. In the central region, where the energy density is the highest, a new state of matter - the quark-gluon plasma - is supposedly created. Afterwards, the plasma expands and cools down, quarks combine into hadrons and their mutual interactions cease when the system reaches the *freeze-out* temperature. Finally, free hadrons created in this process move towards the detectors.

On the right side of the Figure 1.7 a space-time evolution of a collision process is presented, plotted in the light-cone variables ( $z$ ,  $t$ ). The two highly relativistic nuclei are traveling basically along the light cone until they collide at the centre of the diagram. Nuclear fragments emerge from the collision again along the (forward) light cone, while the matter between fragmentation zones populates the central region. This hot and dense matter is believed to be in the state of the quark-gluon plasma. Nowadays, there are several frameworks describing this transition to the QGP phase, for example: QCD string breaking, QCD parton cascades or colour glass condensate evolving into glasma [10].

**String breaking** – In the string picture, the nuclei pass through each other forming colour strings. This is analogous to the situation depicted in the Fig 1.2 - the colour string is created between quarks inside particular nucleons in nuclei. In the next step strings break forming quarks and gluons or directly hadrons. However, at very high energies, when the strings overlap and cannot be treated as independent objects this approach becomes invalid

**Parton cascade** – The parton<sup>4</sup> cascade model is based on the pQCD. The colliding nuclei are treated as clouds of quarks penetrating through each other. The key element of this method is the time evolution of the parton phase-space distributions, which is governed by a relativistic Boltzmann equation with a collision term that contains dominant perturbative QCD interactions. The bottleneck of the parton cascade model is the low energies regime, where the  $Q^2$  is too small to be described by the perturbative theory.

**Colour glass condensate** – The colour glass condensate assumes, that the hadron can be considered as a tightly packed system of interacting gluons. The saturation of gluons increases with energy, hence the total number of gluons may rise without bound. Such a saturated and weakly coupled gluon system is called a colour glass condensate. The fast gluons in the condensate are Lorentz contracted and redistributed on the two very thin sheets representing two colliding nuclei. These sheets are perpendicular to the beam axis. The fast gluons produce mutually orthogonal colour magnetic and electric fields, that only exist on the sheets. Immediately after the collision, i.e. just after the passage of the two gluonic sheets through each other, the longitudinal electric and magnetic fields are produced forming the *glasma*. The glasma fields decay through the classical rearrangement of the fields into radiation of gluons. Also decays due to the quantum pair creations are possible. In this way, the quark-gluon plasma is also produced.

Interactions within the created quark-gluon plasma bring the system into the local statistical equilibrium, hence its further evolution can be described by the relativistic hydrodynamics. The hydrodynamic expansion causes the system to become more and more dilute. The phase transition from the quark-gluon plasma to the hadronic gas occurs. Further expansion causes a transition from the strongly interacting hadronic gas to weakly interacting system of hadrons which move freely to the detectors. Such decoupling of hadrons is called the *freeze-out*. The freeze-out can be divided into two phases: the chemical freeze-out and the thermal one. The *chemical freeze-out* occurs when the inelastic collisions between constituents of the hadron gas stop. As the system evolves from the chemical freeze-out to the thermal one the dominant processes are elastic collisions (for example  $\pi + \pi \rightarrow \rho \rightarrow \pi + \pi$ ) and strong decays of heavier resonances<sup>5</sup> which populate the yield of stable hadrons. Thus, the *thermal freeze-out* is the stage of the evolution of matter, when the strongly coupled system transforms to a weakly coupled one (consisting of essentially free particles). In other words

<sup>4</sup>A parton is a common name for a quark and a gluon.

<sup>5</sup>Resonance is other name for an unstable particle.

this is the moment, where the hadrons practically stop to interact. Obviously, the temperatures corresponding to the two freeze-outs satisfy the condition

$$T_{chem} > T_{therm}, \quad (1.2)$$

where  $T_{chem}$  is the temperature of the chemical freeze-out (inferred from the ratios of hadron multiplicities), and  $T_{therm}$  is the temperature of the thermal freeze-out (obtained from the investigation of the transverse-momentum spectra) [10].

### 1.3.2 QGP signatures

The quark-gluon plasma is a very short living and unstable state of matter. There is no possibility to investigate the properties of a plasma and confirm its existence directly. Hence, several experimental effects were proposed as QGP signatures, some of them have been already observed in heavy ion experiments [8]. As matter created in the heavy ions collisions is supposed to behave like a fluid, one should expect the appearance of collective behaviour at small transverse momenta - so called *elliptic flow* and *radial flow*. The next signal is the temperature range obtained from the measurements of *direct photons*, which gives us information that the system created in heavy ion collisions is far above the critical temperature obtained from the LQCD calculations. The *puzzle in the di-lepton spectrum* can be explained by the modification of spectral shape of vector mesons (mostly  $\rho$  meson) in the presence of a dense medium. This existence of a medium can also shed light on the *jet quenching* phenomenon - the suppression occurrence in the high  $p_T$  domain.

#### Elliptic flow

In a non-central heavy ion collisions, created region of matter has an almond shape with its shorter axis in the *reaction plane* (Fig. 1.8). The pressure gradient

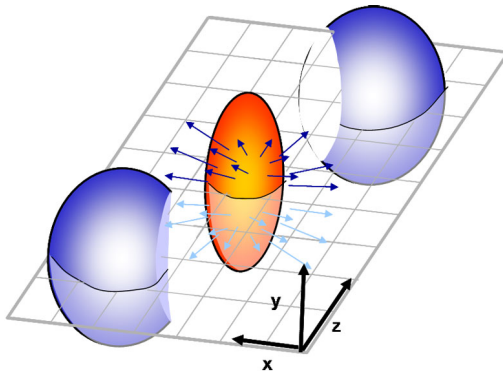


Figure 1.8: Overlapping region which is created in heavy ion collisions has an almond shape. Visible x-z plane is a *reaction plane*. The x-y plane is a *transverse plane*. The z is a direction of the beam [11].

is much larger in-plane rather than out-of-plane. Thus, larger acceleration and transverse velocities are visible in-plane. Such differences can be investigated by studying the distribution of particles with respect to the reaction plane orientation [12]:

$$E \frac{d^3 N}{dp^3} = \frac{1}{2\pi} \frac{d^2 N}{p_T dp_T dy} (1 + 2v_1 \cos(\phi) + 2v_2 \cos(2\phi) + \dots), \quad (1.3)$$

where  $\phi$  is the angle between particle transverse momentum  $p_T$  (a momentum projection on a transverse plane) and the reaction plane,  $E$  is an energy of a particle and  $N$  is their number. The  $y$  variable is *rapidity* defined as:

$$y = \frac{1}{2} \ln \left( \frac{E + p_L}{E - p_L} \right), \quad (1.4)$$

where  $p_L$  is a longitudinal component of a momentum (parallel to the beam direction). The  $v_n$  coefficients indicate the shape of a system. For the most central collisions ( $b = 0$  - see Fig. 1.9) all coefficients vanish  $\sum_{n \in N_+} v_n = 0$  (the overlapping region has the spherical shape). The Fourier series elements in the parentheses in Eq. 1.3 correspond different kinds of flow. The first value "1" represents the *radial flow* - an isotropic flow in every direction. Next coefficient  $v_1$  is responsible for *direct flow* while the  $v_2$  is a measure of elliptic anisotropy (*elliptic flow*). The  $v_2$  has to build up in the early stage of a collision - later the system becomes too dilute: space asymmetry and the pressure gradient vanish. Therefore, the observation of elliptic flow means that the created matter was in fact strongly interacting.

The  $v_2$  coefficient was already measured at CERN SPS, LHC and RHIC. For the first time, hydrodynamics successfully described the collision dynamics as

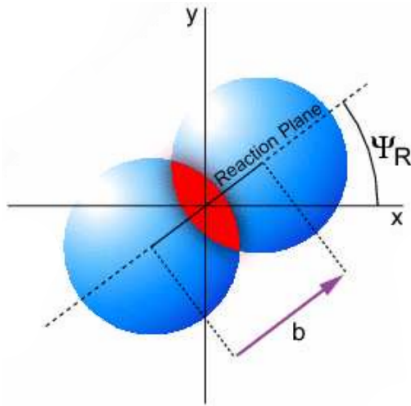


Figure 1.9: Cross-section of a heavy ion collision in a transverse plane. The  $b$  parameter is an *impact parameter* - a distance between centers of nuclei during a collision. An impact parameter is related with the centrality of a collision and a volume of the quark-gluon plasma [12].

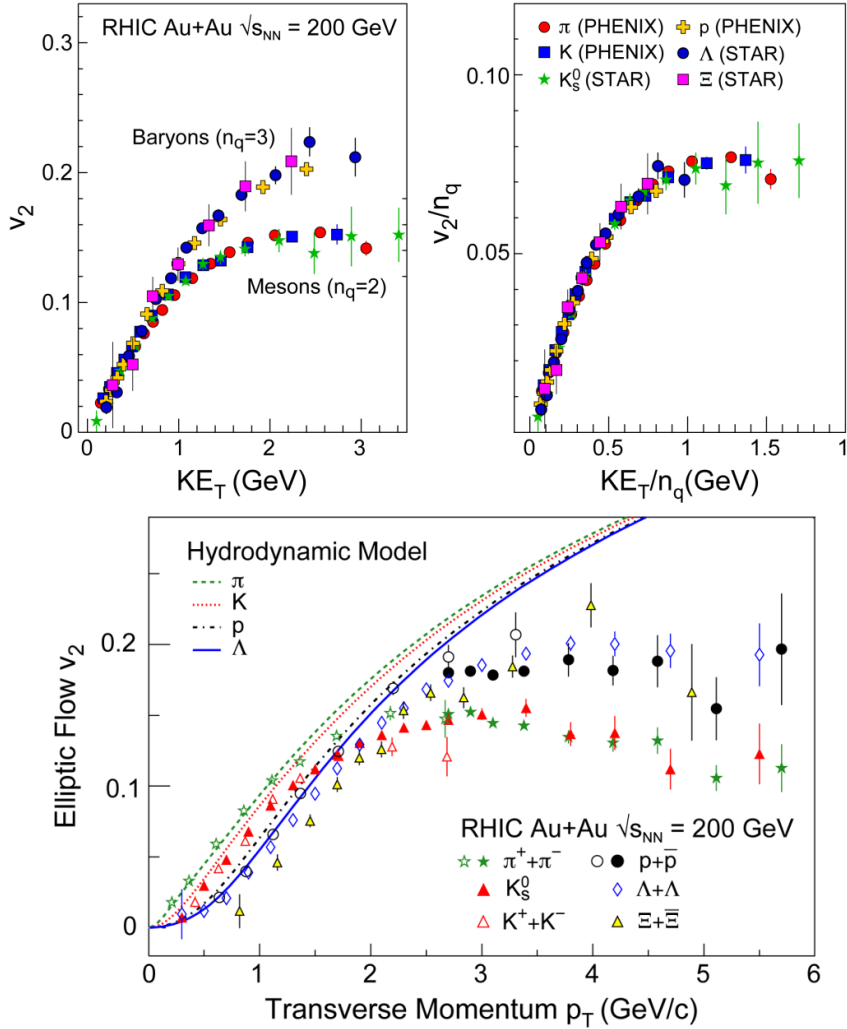


Figure 1.10: *Lower:* The elliptic flow  $v_2$  follows the hydrodynamical predictions for an ideal fluid perfectly. Note that > 99% of all final hadrons have  $p_T < 1.5$  GeV/c. *Upper left:* The  $v_2$  plotted versus transverse kinetic energy  $KE_T = m_T - m_0 = \sqrt{p_T^2 + m_0^2} - m_0$ . The  $v_2$  follows different universal curves for mesons and baryons. *Upper right:* When scaled by the number of valence quarks, the  $v_2$  follows the same universal curve for all hadrons and for all values of scaled transverse kinetic energy [13].

the measured  $v_2$  reached hydrodynamic limit (Fig. 1.10). As expected, there is a mass ordering of  $v_2$  as a function of  $p_T$  (lower plot in the Fig. 1.10) with pions having the largest anisotropy and protons the smallest one. In the upper plots in the Fig. 1.10 there is a  $v_2$  as a function of transverse kinetic energy. The left plot shows two universal trend lines for baryons and mesons. After the scaling of  $v_2$

and the kinetic energy by the number of valence quarks, all of the hadrons follow the same universal curve. Those plots prove that strong collectivity is observed in heavy ion collisions.

### Transverse radial flow

The elliptic flow, described previously, is caused by the pressure gradient, which must also produce a more simple collective behaviour of matter - a movement inside-out, called radial flow. As a result, particles are pushed to higher momenta and they move away from the center of the collision. A source not showing collective behaviour, like pp collisions, produces particle spectra that can be fitted by a power-law [8]:

$$\frac{1}{2\pi p_T} \frac{d^2N}{dp_T d\eta} = C \left( 1 + \frac{p_T}{p_0} \right)^{-n} . \quad (1.5)$$

The  $\eta$  variable is *pseudorapidity* defined as follows:

$$\eta = \frac{1}{2} \ln \left( \frac{p + p_L}{p - p_L} \right) = -\ln \left( \frac{\theta}{2} \right) , \quad (1.6)$$

where  $\theta$  is an emission angle:  $\cos \theta = p_L/p$ .

The hydrodynamical expansion of a system gives the same flow velocity kick for different kinds of particles - ones with bigger masses will gain larger  $p_T$

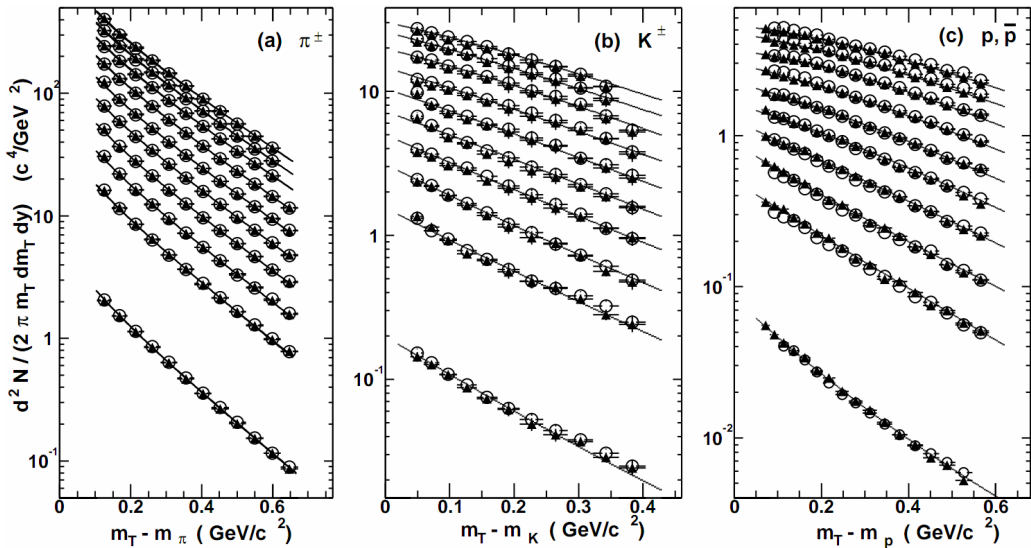


Figure 1.11: Invariant yield of particles versus transverse mass  $m_T = \sqrt{p_T^2 + m_0^2}$  for  $\pi^\pm$ ,  $K^\pm$ ,  $p$  and  $\bar{p}$  at mid-rapidity for p+p collisions (bottom) and Au+Au events from 70-80% (second bottom) to 0-5% (top) centrality [14].

boost. This causes an increase of the yield of particles with larger transverse momenta. In the invariant yield plots (Fig. 1.11) one can observe the decrease of the slope parameter, especially for the heavier hadrons. The spectra of kaons (b) and protons (c) are most affected. One can notice the decrease of the slope parameter for heavy ion collisions (plots from second bottom to top) compared to the proton-proton collisions (bottom ones), where boost from radial flow should not occur [8].

Another signature of a transverse radial flow is a dependence of HBT radii on a pair transverse momentum. Detailed description of this effect is presented in Section 3.4.

### Direct photons

The direct photons are photons, which are not coming from the final state hadrons decays. They can be emitted in different interactions between charged particles created in the collision, either at the partonic or at the hadronic level. Direct photons are considered to be an excellent probe of the early stage of the collision. It is the result of the fact that their mean free path is very large in comparison to the size of the system created in the collision. Thus, photons created at the early stage leave the system without suffering any interaction and retain

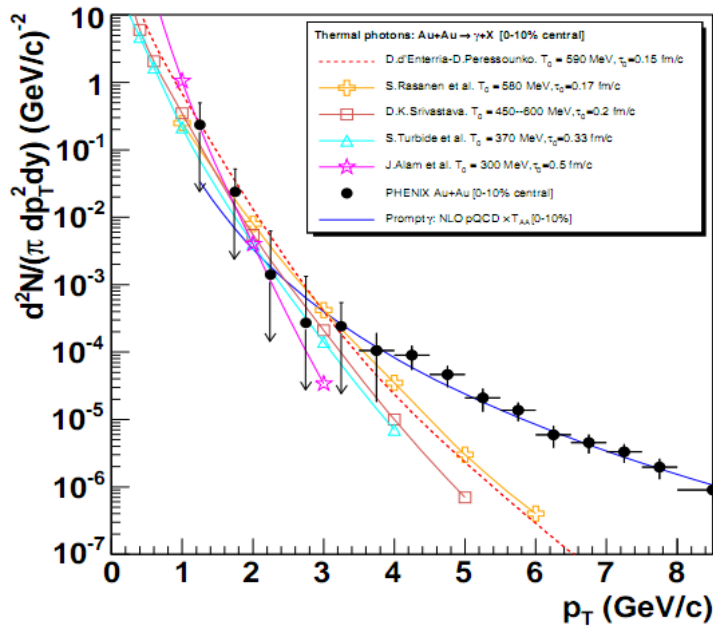


Figure 1.12: Thermal photons spectra for the central Au+Au collisions at  $\sqrt{s_{NN}} = 200$  GeV computed within different hydrodynamical models compared with the pQCD calculations (solid line) and experimental data from PHENIX (black dots) [15].

information about this stage, in particular about its temperature.

One can distinguish two kinds of direct photons: *thermal* and *prompt*. Thermal photons can be emitted from the strong processes in the quark-gluon plasma involving quarks and gluons or hot hadronic matter (e.g. processes:  $\pi\pi \rightarrow \rho\gamma$ ,  $\pi\rho \rightarrow \pi\gamma$ ). They can be observed in the low  $p_T$  region. Prompt photons are believed to come from “hard” collisions of initial state partons belonging to the colliding nuclei. They will dominate the high  $p_T$  region and can be described using the pQCD. The analysis of transverse momentum of spectra of direct photons revealed that the temperature of the source of thermal photons produced in heavy ion collisions at RHIC is in the range of 300-600 MeV (Fig. 1.12). Hence, the direct photons had to come from a system whose temperature is far above the critical temperature for QGP creation.

### Puzzle in di-lepton mass spectrum

The invariant mass spectra (Fig. 1.13) of lepton pairs reveal many peaks corresponding to direct decays of various mesons into a lepton pairs. The continuous background in this plot is caused by the decays of hadrons into more than two leptons (including so-called *Dalitz decays* into a lepton pair and a photon). Particular hadron decay channels, which contribute to this spectrum are shown in Fig. 1.13 with the coloured lines. The sum of various components (called “*the hadronic cocktail*”) is represented by the black line. It describes experimental spectra coming from the simple collisions (like p+p or p+A) quite well with the statistical and systematical uncertainties [9]. However, this situation is different con-

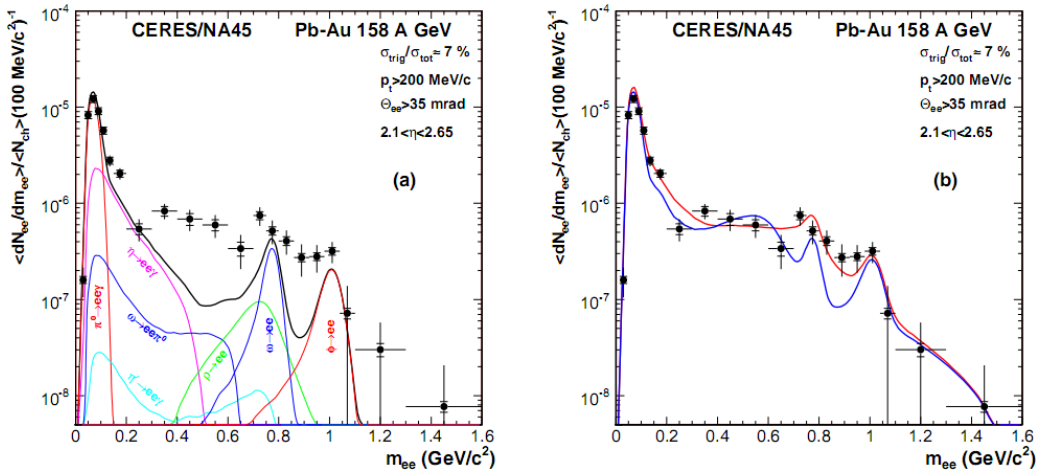


Figure 1.13: Left: Invariant mass spectrum of  $e^+ - e^-$  pairs in  $Pb+Au$  collisions at  $158A$  GeV compared to the sum coming from the hadron decays predictions. Right: The expectations coming from model calculations which assume a drop of the  $\rho$  mass (blue) or a spread of the  $\rho$  width in the medium [16].

sidering more complicated systems i.e. A+A. Exemplary spectra coming from Pb+Au collisions are presented in the plots in Fig. 1.13. The “hadronic cocktail” does not describe the data in the mass range between the  $\pi$  and the  $\rho$  mesons. One can observe a significant excess of electron pairs over the calculated sum in this region. Theoretical explanation of this phenomenon assumes modification of the spectral shape of vector mesons in a dense medium. Two different interpretations of this increase were proposed: a decrease of meson’s mass with the medium density and increase of the meson’s width in the dense medium. In principle, one could think of simultaneous occurrence of both effects: mass shift and resonance broadening. Experimental results coming from the CERES disfavour the mass shift hypothesis indicating only broadening of resonance peaks (Fig. 1.13b) [9].

### Jet quenching

A jet is defined as a group of particles with high energies and close vector momenta. It has its beginning when the two partons are going in opposite directions and have energy big enough to produce new quark-antiquark pair and then radiate gluons. This process can be repeated many times and as a result two back-to-back jets of hadrons are created. It has been found that jets in the opposite hemisphere (*away-side jets*) show a very different pattern in d+Au and Au+Au collisions. This is presented in the azimuthal correlations in the Fig. 1.14. In d+Au collisions, like in p+p, a pronounced away-side jet appears around  $\Delta\phi = \pi$  - exactly opposite to the trigger jet, which is typical for di-jet events. However, in

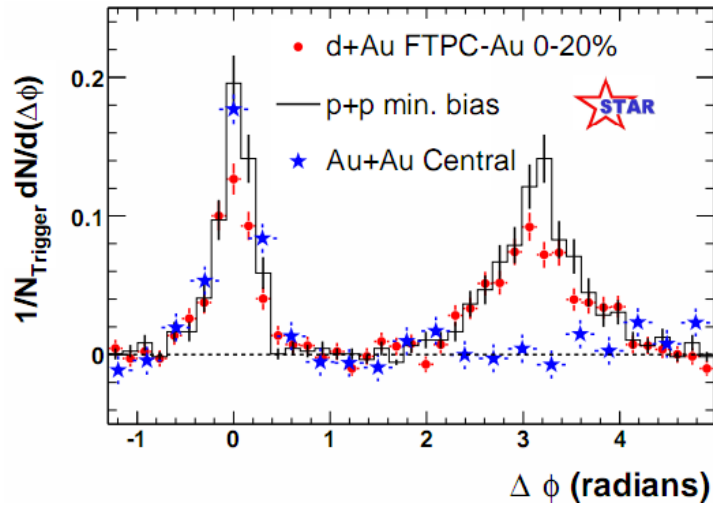


Figure 1.14: Azimuthal angle difference  $\Delta\phi$  distributions for different colliding systems at  $\sqrt{s_{NN}} = 200$  GeV. Transverse momentum cut:  $p_T > 2$  GeV. For the Au+Au collisions the away-side jet is missing [17].

the case of central Au+Au collisions the away-side jet is suppressed. When the jet has its beginning near the surface of the quark-gluon plasma, one of the jets (*near-side jet*) leaves the system almost without any interactions. This jet is visible in the correlation plot as a high peak at  $\Delta\phi = 0$ . However, the jet which moves towards the opposite direction has to penetrate a dense medium. The interaction with the plasma causes energy dissipation of particles and is visible on an azimuthal correlation plot as a disappearance of the away-side jet [9].

# Chapter 2

## Therminator model

THERMINATOR [18] is a Monte Carlo event generator designed to investigate the particle production in the relativistic heavy ion collisions. The functionality of the code includes a generation of the stable particles and unstable resonances at the chosen hypersurface model. It performs the statistical hadronization which is followed by space-time evolution of particles and the decay of resonances. The key element of this method is an inclusion of a complete list of hadronic resonances, which contribute very significantly to the observables. The second version of THERMINATOR [19] gives a possibility to utilize any shape of freeze-out hypersurface and the expansion velocity field, especially those generated externally with various hydrodynamic codes. The event generator is written in C++ programming language and it employs ROOT [20] analysis framework.

### 2.1 (3+1)-dimensional viscous hydrodynamics

Most of the relativistic viscous hydrodynamic calculations are done in (2+1)-dimensions. Such simplification assumes boost-invariance of a matter created in a collision. Experimental data reveal that no boost-invariant region is formed in the collisions [21]. Hence, for the better description of created system a (3+1)-dimensional model is required.

In the four dimensional relativistic dynamics one can describe a system using a space-time four-vector  $x^\nu = (ct, x, y, z)$ , a velocity four-vector  $u^\nu = \gamma(c, v_x, v_y, v_z)$  and an energy-momentum tensor  $T^{\mu\nu}$ . The particular components of  $T^{\mu\nu}$  have a following meaning:

- $T^{00}$  - energy density,
- $cT^{0\alpha}$  - energy flux across a surface  $x^\alpha$ ,
- $T^{\alpha 0}$  -  $\alpha$ -momentum flux across a surface  $x^\alpha$  multiplied by  $c$ ,
- $T^{\alpha\beta}$  - components of momentum flux density tensor,

where  $\gamma = (1 - v^2/c^2)^{-1/2}$  is the Lorentz factor and  $\alpha, \beta \in \{1, 2, 3\}$ .  $T^{\mu\nu}$  can be expressed using  $u^\nu$  as follows [22]:

$$T_0^{\mu\nu} = (e + p)u^\mu u^\nu - pg^{\mu\nu} \quad (2.1)$$

where  $e$  is an energy density,  $p$  is a pressure and  $g^{\mu\nu}$  is an inverse metric tensor:

$$g^{\mu\nu} = \begin{bmatrix} 1 & 0 & 0 & 0 \\ 0 & -1 & 0 & 0 \\ 0 & 0 & -1 & 0 \\ 0 & 0 & 0 & -1 \end{bmatrix}. \quad (2.2)$$

The presented version of the energy-momentum tensor (Eq. 2.1) can be used to describe dynamics of a perfect fluid. To take into account influence of viscosity, one has to apply the following corrections coming from shear  $\pi^{\mu\nu}$  and bulk  $\Pi$  viscosities [23]:

$$T^{\mu\nu} = T_0^{\mu\nu} + \pi^{\mu\nu} + \Pi(g^{\mu\nu} - u^\mu u^\nu). \quad (2.3)$$

The stress tensor  $\pi^{\mu\nu}$  and the bulk viscosity  $\Pi$  are solutions of dynamical equations in the second order viscous hydrodynamic framework [22]. The comparison of hydrodynamic calculations with the experimental results reveals that the shear viscosity divided by entropy  $\eta/s$  has to be small and close to the AdS/CFT estimate  $\eta/s = 0.08$  [23, 24]. The bulk viscosity over entropy value used in calculations is  $\zeta/s = 0.04$  [23].

In the situation, when the system described by  $T^{\mu\nu}$  is evolving close to local thermodynamic equilibrium, the relativistic hydrodynamic equations take the following form:

$$\partial_\mu T^{\mu\nu} = 0, \quad (2.4)$$

which can be used to determine the dynamics of the local energy density, pressure and flow velocity.

Hydrodynamic calculations are starting from the Glauber<sup>1</sup> model initial conditions. The collective expansion of a fluid ends at the freeze-out hypersurface. That surface is usually defined as a constant temperature surface, or equivalently as a cut-off in local energy density. The freeze-out is assumed to occur at the temperature  $T = 140$  MeV.

## 2.2 Statistical hadronization

Statistical description of heavy ion collisions has been successfully used to quantitatively characterize the *soft* physics, i.e. the regime with the transverse momentum not exceeding 2 GeV. The basic assumption of the statistical approach of evolution of the quark-gluon plasma is that at some point of the space-time

---

<sup>1</sup>The Glauber Model is used to calculate “geometrical” parameters of a collision like an impact parameter, number of participating nucleons or the number of binary collisions.

evolution of the fireball, the thermal equilibrium is reached. When the system is in this state the local phase-space densities of particles follow the Fermi-Dirac or Bose-Einstein statistical distributions. At the end of the plasma expansion, the freeze-out occurs. The freeze-out model incorporated in THERMINATOR assumes that chemical and thermal freeze-outs occur at the same time.

### 2.2.1 Cooper-Frye formalism

The result of the hydrodynamic calculations is the freeze-out hypersurface  $\Sigma^\mu$ . A three-dimensional element of the surface is defined as [19]

$$d\Sigma_\mu = \epsilon_{\mu\alpha\beta\gamma} \frac{\partial x^\alpha}{\partial \alpha} \frac{\partial x^\beta}{\partial \beta} \frac{\partial x^\gamma}{\partial \gamma} d\alpha d\beta d\gamma, \quad (2.5)$$

where  $\epsilon_{\mu\alpha\beta\gamma}$  is the Levi-Civita tensor and the variables  $\alpha, \beta, \gamma \in \{1, 2, 3\}$  are used to parametrize the three-dimensional freeze-out hypersurface in the Minkowski four-dimensional space. The Levi-Civita tensor is equal to 1 when the indices form an even permutation (eg.  $\epsilon_{0123}$ ), to -1 when the permutation is odd (e.g.  $\epsilon_{2134}$ ) and has a value of 0 if any index is repeated. Therefore [19],

$$d\Sigma_0 = \begin{vmatrix} \frac{\partial x}{\partial \alpha} & \frac{\partial x}{\partial \beta} & \frac{\partial x}{\partial \gamma} \\ \frac{\partial y}{\partial \alpha} & \frac{\partial y}{\partial \beta} & \frac{\partial y}{\partial \gamma} \\ \frac{\partial z}{\partial \alpha} & \frac{\partial z}{\partial \beta} & \frac{\partial z}{\partial \gamma} \end{vmatrix} d\alpha d\beta d\gamma \quad (2.6)$$

while the remaining components are obtained by cyclic permutations of  $t, x, y$  and  $z$ .

The number of hadrons produced on the hypersurface  $\Sigma^\mu$  can be calculated from the Cooper-Frye formalism. The following integral yields the total number of created particles [19]:

$$N = (2s + 1) \int \frac{d^3 p}{(2\pi)^3 E_p} \int d\Sigma_\mu p^\mu f(p_\mu u^\mu) , \quad (2.7)$$

where  $f(p_\mu u^\mu)$  is the phase-space distribution of particles (for stable ones and resonances). The dependence of the momentum density can be simply derived from Eq. 2.7 [25]:

$$E \frac{d^3 N}{dp^3} = \int d\Sigma_\mu f(p_\mu u^\mu) p^\mu . \quad (2.8)$$

The momentum distribution  $f$  contains non-equilibrium corrections:

$$f = f_0 + \delta f_{shear} + \delta f_{bulk} , \quad (2.9)$$

where

$$f_0(p_\mu u^\mu) = \left\{ \exp \left[ \frac{p_\mu u^\mu - (B\mu_B + I_3\mu_{I_3} + S\mu_S + C\mu_C)}{T} \right] \pm 1 \right\}^{-1} . \quad (2.10)$$

In case of fermions, in the Eq. 2.10 there is a plus sign and for bosons, minus sign respectively. The thermodynamic quantities appearing in the  $f_0(\cdot)$  are  $T$  - temperature,  $\mu_B$  - baryon chemical potential,  $\mu_{I_3}$  - isospin chemical potential,  $\mu_S$  - strange chemical potential,  $\mu_C$  - charmed chemical potential and  $s$  as a spin of the particle. The hydrodynamic calculations yield the flow velocity at freeze-out as well as the stress and bulk viscosity tensors required to calculate non-equilibrium corrections to the momentum distribution used in Eq. 2.7. The term coming from shear viscosity has a form [23]

$$\delta f_{shear} = f_0(1 \pm f_0) \frac{1}{2T^2(e+p)} p^\mu p^\nu \pi_{\mu\nu} \quad (2.11)$$

and bulk viscosity

$$\delta f_{bulk} = C f_0(1 \pm f_0) \left( \frac{(u^\mu p_\mu)^2}{3u^\mu p_\mu} - c_s^2 u^\mu p_\mu \right) \Pi \quad (2.12)$$

where  $c_s$  is sound velocity and

$$\frac{1}{C} = \frac{1}{3} \frac{1}{(2\pi)^3} \sum_{hadrons} \int d^3 p \frac{m^2}{E} f_0(1 \pm f_0) \left( \frac{p^2}{3E} - c_s^2 E \right). \quad (2.13)$$

## 2.3 Event generation procedure

The equations presented in the previous section are directly used in the THERMINATOR to generate the primordial hadrons (created during freeze-out) with the Monte-Carlo method. This procedure consists of 3 main steps, where the first two are performed only once per given parameter set. After the generation of primordial particles, the cascade decay of unstable resonances is performed.

### Determination of a maximum of an integrand

In order to generate particles through a Monte Carlo method, the maximum value of the distribution in the right-hand-side of Eq. 2.7 must be known. To find this number, THERMINATOR generates a sample consisting of a large number of particles. For each particle the value of a distribution is calculated and the maximum value  $f_{max}$  of the sample is stored. A large enough sample of particles guarantees that  $f_{max}$  found in this procedure is a good estimate of the maximum value of a distribution in Eq. 2.7. This maximum value depends on a particle type and values of parameters, but does not change from event to event. Hence this procedure is performed once, at the beginning of the event generation [18].

### Multiplicity calculation

In order to generate events, a multiplicity of each particle must be known. The multiplicities are obtained through a numerical integration of the distribution functions (Eq. 2.7) in the given integration ranges determined by the model parameters. As in the previous case, the multiplicities depend only on the model parameters and they are calculated only once at the beginning of the event generation [18].

### Events and particles generation

Every event produced by THERMINATOR is generated separately. At first, the multiplicities for each of particle type are calculated as random numbers from a Poisson distribution, with the mean being the average particles multiplicity determined in the previous step. Then, the program proceeds to generate particles from the heaviest to the lightest ones. In essence, this procedure is a generation of the set of six random numbers: three components of particle's momentum ( $p_x$ ,  $p_y$ ,  $p_z$ ) and three parameters providing space-time coordinates on a freeze-out hypersurface ( $\zeta$ ,  $\phi_s$ ,  $\theta$ ). The events generation procedure is based on the von Neumann's acceptance-rejection algorithm. Firstly, the integrand in Eq. 2.7 is calculated using given set of numbers. Subsequently, a random number from an uniform distribution over  $[0; f_{max}]$  is compared to the value of the integrand. If it is lower, then the set of numbers is stored as an actual particle. If this condition was not satisfied, a new set is generated. This procedure is repeated until the determined number of particles of each kind is generated. At this point, all primordial particles (stable and resonances) have been generated and stored in the event [18].

### Decays of unstable particles

In the next step of event generation, a simulation of unstable resonances decays is performed. A particle is considered as unstable when it has non-zero width  $\Gamma$  defined in the input files of THERMINATOR. The decays proceed sequentially from the heaviest to the lightest particles. Unstable products of decays are added to the particles generated in the current event and are processed in the subsequent steps. If a particle has several decay channels, one of them is selected randomly with the appropriate probability corresponding to the branching ratio provided in the input files. THERMINATOR in the hadronic cascade process performs two-body and three-body decays.

At the beginning of the cascade decay, the lifetime  $\tau$  of a particle with mass  $M$ , moving with the four-momentum  $p^\mu$ , is generated randomly according to the exponential decay law  $\exp(-\Gamma\tau)$ . When the lifetime is known, the point of its decay is calculated as [18]:

$$x_{decay}^\mu = x_{origin}^\mu + \frac{p^\mu}{M}\tau, \quad (2.14)$$

where  $x_{origin}^\mu$  is a position of unstable particle's creation. At the  $x_{decay}^\mu$  point decay occurs and daughter particles with energies and momenta determined by the conservation laws are generated. Fig. 2.1 illustrates the cascade decay process [18].

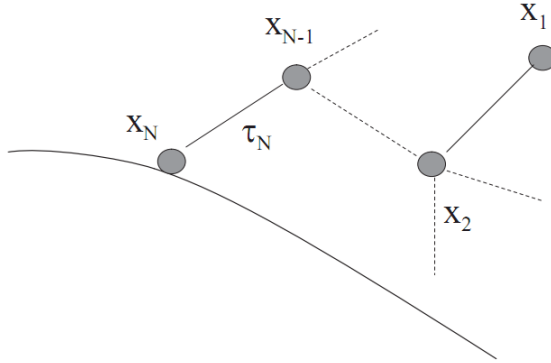


Figure 2.1: The cascade decay in the single freeze-out model. An unstable resonance  $x_N$  is formed at the freeze-out hypersurface and travels for the time  $\tau_N$  depending on its lifetime and decays. If the products are also resonances ( $x_{N-1}, x_2$ ) they decay further until the stable particles are formed ( $x_1$ ) [18].

## Chapter 3

# Particle interferometry

Two-particle interferometry (also called *femtoscopy*) gives a possibility to investigate space-time characteristics of the particle-emitting source created in heavy ion collisions. Through the study of particle correlations, their momentum distributions can be used to obtain information about the spatial extent of the created system. Using this method, one can measure sizes of the order of  $10^{-15}$  m and times of the order of  $10^{-23}$  s.

### 3.1 The HBT interferometry

In 1956, Robert Hanbury Brown and Richard Q. Twiss proposed a method which allowed to investigate angular dimensions of stars through analysis of interference between photons. They performed a measurement of the intensity of a beam of light coming from a star using two detectors separated in space. In a signal plotted as a function of distance between detectors an interference effect was observed. Despite the fact that no phase information was collected, a positive correlation was visible. Hanbury Brown and Twiss used this interference signal to calculate the angular size of a star with excellent resolution. In principle, the HBT interferometry was designed for astronomy purposes, however it can be also used to measure extent of any emitting source. Therefore, it was adapted to heavy ion collisions to investigate dimensions of a particle-emitting source [8].

### 3.2 Theoretical approach

Intensity interferometry in heavy ion physics uses similar mathematical formalism as the astronomy HBT measurement. The difference between them is that femtoscopy uses a two-particle relative momentum and yields the space-time picture of a source, whereas the latter method uses the distance between detectors to calculate angular size of the star.

### 3.2.1 Conventions used

In heavy ion collisions to describe particular directions, components of momentum and location of particles, one uses naming convention called the Bertsch-Pratt coordinate system. This system is presented in Fig. 3.1. The three directions

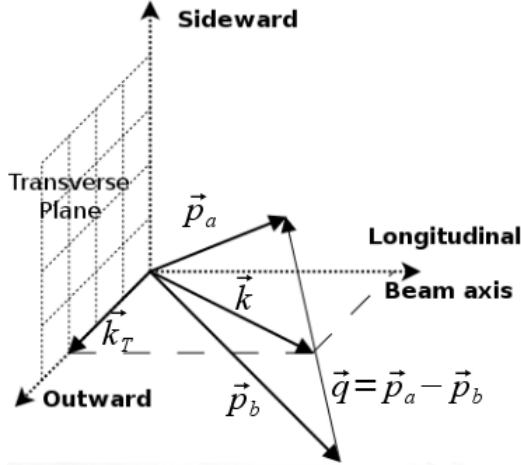


Figure 3.1: Bertsch-Pratt directions naming convention used in heavy ion collision.

are called *longitudinal*, *outward* and *sideward*. The longitudinal direction is parallel to the beam axis. The plane perpendicular to the beam axis is called a *transverse plane*. A projection of a particle pair momentum  $\mathbf{k} = (\mathbf{p}_a + \mathbf{p}_b)/2$  on a transverse plane (a *transverse momentum*  $\mathbf{k}_T$ ) determines the *outward* direction:  $(\mathbf{k})_{out} = \mathbf{k}_T$ . A direction which is perpendicular to the longitudinal and outward ones is called *sideward*.

A particle pair is usually described using two coordinate systems. The first one, *Longitudinally Co-Moving System (LCMS)* is moving along the particle pair with the longitudinal direction in the other words, the pair longitudinal momentum vanishes:  $(\mathbf{p}_a)_{long} = -(\mathbf{p}_b)_{long}$ . The second system is called *Pair Rest Frame (PRF)*. In the PRF the centre of mass rests:  $\mathbf{p}_a = -\mathbf{p}_b$ . Variables which are expressed in the PRF are marked with a star (e.g.  $\mathbf{k}^*$ ).

The transition of space-time coordinates from LCMS to PRF is simply a boost along the outward direction, with the transverse velocity of the pair  $\beta_T = (\mathbf{v}/c)_{out}$  [26]:

$$r_{out}^* = \gamma_T(r_{out} - \beta_T \Delta t), \quad (3.1)$$

$$r_{side}^* = r_{side}, \quad (3.2)$$

$$r_{long}^* = r_{long}, \quad (3.3)$$

$$\Delta t^* = \gamma_T(\Delta t - \beta_T r_{out}), \quad (3.4)$$

where  $\gamma_T = (1 - \beta_T^2)^{-1/2}$  is the Lorentz factor. However, in calculations performed

in this work the equal time approximation is used which assumes that particles in a pair were produced at the same time in PRF - the  $\Delta t^*$  is neglected.

The most important variables used to describe particle pair are total momentum  $\mathbf{P} = \mathbf{p}_a + \mathbf{p}_b$  and relative momentum  $\mathbf{q} = \mathbf{p}_a - \mathbf{p}_b$ . In PRF, the following relation  $\mathbf{q} = 2\mathbf{k}^*$  is also valid, where  $\mathbf{k}^*$  is a momentum of the first particle in PRF.

### 3.2.2 Two particle wave function

Let us consider two identical particles with momenta  $\mathbf{p}_1$  and  $\mathbf{p}_2$  emitted from space points  $\mathbf{x}_1$  and  $\mathbf{x}_2$ . These particles can be treated as two incoherent waves. If the particles are identical, they are also indistinguishable. Therefore, one has

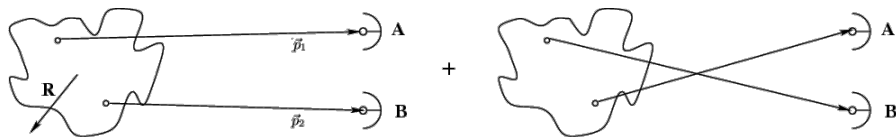


Figure 3.2: The pair wave function is a superposition of all possible states. In case of particle interferometry it includes two cases: particles with momenta  $p_1, p_2$  registered by detectors  $A, B$  and  $p_1, p_2$  registered by  $B, A$  respectively.

also take into account the scenario, where the particle with momentum  $\mathbf{p}_1$  is emitted from  $\mathbf{x}_2$  and particle  $\mathbf{p}_2$  from  $\mathbf{x}_1$  (Fig. 3.2). In such case, the wave function describing behaviour of a pair has to contain both components [8]:

$$\Psi_{ab}(\mathbf{q}) = \frac{1}{\sqrt{2}} [\exp(-i\mathbf{p}_1\mathbf{x}_1 - i\mathbf{p}_2\mathbf{x}_2) \pm \exp(-i\mathbf{p}_2\mathbf{x}_1 - i\mathbf{p}_1\mathbf{x}_2)] . \quad (3.5)$$

While in the case of identical bosons it is symmetric ("+" sign in Eq. 3.5) and in case of identical fermions - antisymmetric ("-" sign). This anti-symmetrization or symmetrization implies the correlation effect coming from the Fermi-Dirac or Bose-Einstein statistics accordingly. The exact wave function forms used in calculations in this work are given by:

$$|\Psi_{\pi\pi}(\mathbf{r}^*, \mathbf{k}^*)|^2 = |\Psi_{KK}(\mathbf{r}^*, \mathbf{k}^*)|^2 = 1 + \cos(2\mathbf{k}^*\mathbf{r}^*) , \quad (3.6)$$

$$|\Psi_{pp}(\mathbf{r}^*, \mathbf{k}^*)|^2 = 1 - \frac{1}{2} \cos(2\mathbf{k}^*\mathbf{r}^*) . \quad (3.7)$$

The first one is used in the case of identical bosons, and the latter one is for identical fermions. A wave function for pair of spin-1/2 fermions (Eq. 3.7) is a superposition of two possible states: singlet state (with spin equal to 0 and one eigenstate) and triplet state (with spin equal to 1 and three possible eigenstates). For the singlet state, a wave function is symmetric and for the triplet state, it is antisymmetric. In other words, the  $|\Psi_{pp}|^2$  encodes correlation coming from Bose-Einstein statistics (with weight 1/4) and anti-correlation from Fermi-Dirac distribution (with weight 3/4).

In femtoscopy one usually performs full analysis of a correlation function through the comparison to its analytical form. In this case, the pair wave function has to include all kinds of interactions between particles. However, the aim of this work is an analysis of femtoscopic radii proportional to the inverse of a width of a correlation function (for detailed description see Section 3.2.4). This width is determined by effects coming from quantum statistics. Besides, the influence of other effects (like Final State Interactions) on femtoscopic radius is small. Moreover, the inclusion of Final State Interactions in computation increase its complexity and required time. Hence, one can calculate the correlation function using only the quantum statistics and still be able to extract femtoscopic information.

### 3.2.3 Source emission function

To describe a particle emitting source, one uses a single-particle emission function [26]:

$$S_A(\mathbf{x}_1, \mathbf{p}_1) = \int S(\mathbf{x}_1, \mathbf{p}_1, \mathbf{x}_2, \mathbf{p}_2, \dots, \mathbf{x}_N, \mathbf{p}_N) d\mathbf{x}_2 d\mathbf{p}_2 \dots d\mathbf{x}_N d\mathbf{p}_N \quad (3.8)$$

and a two-particle one:

$$S_{AB}(\mathbf{x}_1, \mathbf{p}_1, \mathbf{x}_2, \mathbf{p}_2) = \int S(\mathbf{x}_1, \mathbf{p}_1, \mathbf{x}_2, \mathbf{p}_2, \dots, \mathbf{x}_N, \mathbf{p}_N) d\mathbf{x}_3 d\mathbf{p}_3 \dots d\mathbf{x}_N d\mathbf{p}_N . \quad (3.9)$$

Emission function  $S(\cdot)$  can be interpreted as a probability to emit a particle, or a pair of particles from a given space-time point with a certain momentum. In principle, the source function should encode all physics aspects of the particle generation process i.e. the symmetrization for bosons and fermions, as well as the two-body and many body Final State Interactions. Instead of this, one usually assumes that each particle's emission process is independent - the interaction between final-state particles after their creation is not related with their generation process. This assumption allows to construct two-particle emission function from single particle emission functions via a convolution [26]:

$$\begin{aligned} S(\mathbf{k}^*, \mathbf{r}^*) &= \int S_A(\mathbf{p}_1, \mathbf{x}_1) S_B(\mathbf{p}_2, \mathbf{x}_2) \delta \left[ \mathbf{k}^* - \frac{\mathbf{p}_1 + \mathbf{p}_2}{2} \right] \delta [\mathbf{r}^* - (\mathbf{x}_1 - \mathbf{x}_2)] \\ &\quad \times d^4 \mathbf{x}_1 d^4 \mathbf{x}_2 d^4 \mathbf{x}_1 d^3 \mathbf{p}_1 d^3 \mathbf{p}_2 . \end{aligned} \quad (3.10)$$

In principle, Eq. 3.10 is not reversible - an information about  $S_A(\cdot)$  cannot be derived from  $S_{AB}(\cdot)$ . In the case of identical particles ( $S_A = S_B$ ), one can make further simplifications. Femtoscopy can give information only about two-particle emission function. Moreover, convolution of the two identical Gaussian distributions is also a Gaussian distribution with  $\sigma$  multiplied by  $\sqrt{2}$ . Hence, when considering Gaussian distribution as a source function in Eq. 3.10, one can obtain a  $\sigma$  of a single emission function from a two-particle one. Considering pairs of

identical particles, an emission function is assumed to be described by the following equation in Pair Rest Frame [26]:

$$S_{1D}^{PRF}(\mathbf{r}^*) = \exp\left(-\frac{{r_{out}^*}^2 + {r_{side}^*}^2 + {r_{long}^*}^2}{4{R_{inv}}^2}\right). \quad (3.11)$$

To make a transition from the three-dimensional variables to the one-dimensional variables, the proper Jacobian is required  $r^{*2}$ :

$$\boxed{S_{1D}^{PRF}(r^*) = r^{*2} \exp\left(-\frac{r^{*2}}{4{R_{inv}}^2}\right)}. \quad (3.12)$$

The “4” in the denominator before the  $R_{inv}$  in Eq. 3.12 comes from the convolution of the two Gaussian distributions, which multiplies the  $R_{inv}$  by a factor of  $\sqrt{2}$ .

The emission function in a more complex form was used by all RHIC and SPS experiments in identical pion femtoscopy:

$$\boxed{S_{3D}^{LCMS}(\mathbf{r}) = \exp\left(-\frac{{r_{out}}^2}{4{R_{out}}^2} - \frac{{r_{side}}^2}{4{R_{side}}^2} - \frac{{r_{long}}^2}{4{R_{long}}^2}\right)}. \quad (3.13)$$

The main difference is that it contains three different and independent widths  $R_{out}$ ,  $R_{side}$ ,  $R_{long}$  and they are defined not in PRF, but in LCMS. Unlike in PRF, in LCMS an equal-time approximation is not used. For identical particles this is not a problem - only Coulomb interaction inside a wave function depends on  $\Delta t$ .

### **Relationship between one-dimensional and three-dimensional source sizes**

Up to now, most of femtoscopic measurements were limited only to averaged source size  $R_{av}^L$  (the letter “L” in superscript stands for LCMS):

$$S_{1D}^{LCMS}(\mathbf{r}) = \exp\left(-\frac{{r_{out}}^2 + {r_{side}}^2 + {r_{long}}^2}{2{R_{av}^L}^2}\right). \quad (3.14)$$

The relationship between  $S_{1D}^{LCMS}(\cdot)$  and  $S_{3D}^{LCMS}(\cdot)$  is given by:

$$\begin{aligned} S_{3D}^{LCMS}(r) &= \int \exp\left(-\frac{{r_{out}}^2}{2{R_{out}^L}^2} - \frac{{r_{side}}^2}{2{R_{side}^L}^2} - \frac{{r_{long}}^2}{2{R_{long}^L}^2}\right) \\ &\times \delta\left(r - \sqrt{{r_{out}}^2 + {r_{side}}^2 + {r_{long}}^2}\right) dr_{out} dr_{side} dr_{long}. \end{aligned} \quad (3.15)$$

The one-dimensional source size corresponding to the three-dimensional one can be approximated by the following form:

$$S_{1D}^{LCMS}(r) = r^2 \exp\left(-\frac{r^2}{2{R_{av}^L}^2}\right). \quad (3.16)$$

The above equation assumes that  $R_{out}^L = R_{side}^L = R_{long}^L$  hence  $R_{av}^L = R_{out}^L$ . If the last condition is not satisfied, one can not give an explicit mathematical relation between one-dimensional and three-dimensional source sizes. However, for realistic values of  $R$  (i.e. for similar values of  $R_{out}$ ,  $R_{side}$ ,  $R_{long}$ ), the  $S_{3D}^{LCMS}$  from Eq. 3.15 is not very different from Gaussian distribution and can be well approximated by Eq. 3.16.

A deformation of an averaged source function caused by big differences between  $R_{out}$ ,  $R_{side}$ ,  $R_{long}$  is presented in the Fig. 3.3. A three-dimensional Gaussian distribution with varying widths was projected into one-dimensional function using the Eq. 3.15. Afterwards, an one-dimensional Gaussian distribution was fitted. One can notice a heavy tail of an averaged distribution in the large  $r$  region, which makes this approximation using one-dimensional distribution in this case quite inaccurate.

One can obtain a relation between one-dimensional width and three-dimensional ones from Eq. 3.15 and Eq. 3.16 through numerical calculations [26]:

$$R_{av}^L = \sqrt{\left(R_{out}^L{}^2 + R_{side}^L{}^2 + R_{long}^L{}^2\right)/3}. \quad (3.17)$$

This equation does not depend on the pair velocity, hence it is valid both in LCMS and PRF.

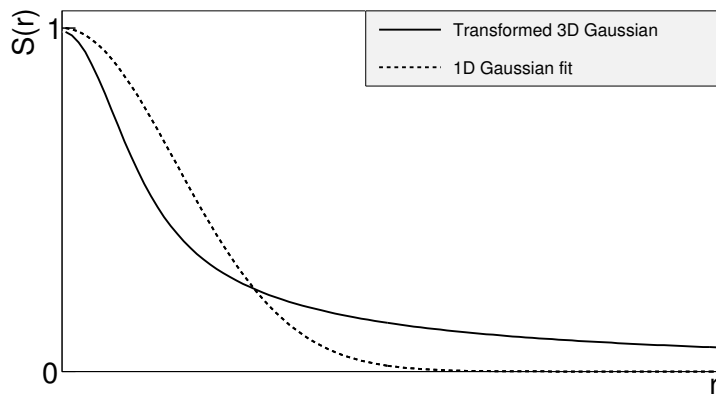


Figure 3.3: A three-dimensional Gaussian source function with different widths was transformed into one-dimensional function. To illustrate deformations, one-dimensional Gaussian distribution was fitted.

### 3.2.4 Analytical form of a correlation function

The fundamental object in a particle interferometry is a correlation function defined as:

$$C(\mathbf{p}_a, \mathbf{p}_b) = \frac{P_2(\mathbf{p}_a, \mathbf{p}_b)}{P_1(\mathbf{p}_a)P_1(\mathbf{p}_b)}, \quad (3.18)$$

where  $P_2$  is a conditional probability to observe a particle with momentum  $\mathbf{p}_b$  if particle with momentum  $\mathbf{p}_a$  was also observed, while a  $P_1$  is a probability to register a particle with a given momentum. The relationship between source emission function, pair wave function and the correlation function is described by the following equation:

$$C(\mathbf{p}_1, \mathbf{p}_2) = \int S_{AB}(\mathbf{p}_1, \mathbf{x}_1, \mathbf{p}_2, \mathbf{x}_2) |\Psi_{AB}|^2 d^4\mathbf{x}_1 d^4\mathbf{x}_2. \quad (3.19)$$

Substituting the one-dimensional emission function (Eq. 3.12) into the above equation leads to the following form of correlation function in PRF:

$$\boxed{C(q) = 1 + \lambda \exp(-R_{inv}^2 q^2)}, \quad (3.20)$$

where  $q$  is a momentum difference between two particles. On the other hand, using the three-dimensional emission function (Eq. 3.13) one gets the following correlation function defined in LCMS:

$$\boxed{C(\mathbf{q}) = 1 + \lambda \exp(-R_{out}^2 q_{out}^2 - R_{side}^2 q_{side}^2 - R_{long}^2 q_{long}^2)}, \quad (3.21)$$

where  $q_{out}$ ,  $q_{side}$ ,  $q_{long}$  are  $\mathbf{q}$  components in the outward, sideward and longitudinal directions. The  $\lambda$  parameter in the above equations determines the correlation strength. In principle, the  $\lambda$  coefficient has values in the range  $\lambda \in [-0.5, 1]$  which depends on the pair type. In the case of pairs of identical bosons (like  $\pi-\pi$  or  $K-K$ ) the  $\lambda \rightarrow 1$  while for identical fermions (e.g.  $p-p$ )  $\lambda \rightarrow -0.5$ . Values of  $\lambda$  observed experimentally are lower than 1 (for bosons) and greater than -0.5 (for fermions). There are few explanations to this effect: detector's efficiencies, inclusion of misidentified particles in a used sample or inclusion of non-correlated pairs (when one or both particles come from e.g. long-lived resonance). The analysis carried out in this work uses data from a model, therefore the detector efficiency and particle's purity is not taken into account [26].

### 3.2.5 Spherical harmonics decomposition of a correlation function

The results coming from an analysis using three-dimensional correlation function in Cartesian coordinates are quite difficult to visualize. To do that, one usually performs a projection into one dimension in outward, sideward and longitudinal directions. However, important information about a correlation function may be lost in this procedure, because it gives only a limited view of the

full three-dimensional structure. Recently, a more advanced way of presenting correlation function - a spherical harmonics decomposition, was proposed. In this method, the three-dimensional correlation function is decomposed into an infinite set of components in a form of one-dimensional histograms  $C_l^m(q)$ . In this representation, a correlation function is defined as a sum of a series [27]:

$$C(\mathbf{q}) = \sum_{l,m} C_l^m(q) Y_l^m(\theta, \phi). \quad (3.22)$$

Spherical harmonics  $Y_l^m(\theta, \phi)$  are an orthogonal set of solutions to the Laplace's equation in spherical coordinates. Hence, in this approach, a correlation function is defined as a function of  $q$ ,  $\theta$  and  $\phi$ . To obtain  $C_l^m$  coefficients in the series, one has to calculate the following integral:

$$C_l^m(q) = \int_{\Omega} C(q, \theta, \phi) Y_l^{m*}(\theta, \phi) d\Omega, \quad (3.23)$$

where  $\Omega$  is a full solid angle.

Spherical harmonics representation has several important advantages. First of all, it requires less statistics than traditional analysis performed in Cartesian coordinates. Moreover, it encodes full three-dimensional information in a set of one-dimensional plots. However, the full description of a correlation function requires infinite number of  $l$  and  $m$  components. But it so happens that the intrinsic symmetries of a pair distribution in a femtoscopic analysis result in a fact that most of the components vanish. For the identical particles correlation function, all coefficients with odd values of  $l$  and  $m$  disappear. It has been also shown that the most significant portion of femtoscopic data is stored in the components with the lowest  $l$  values. It is expected that the main femtoscopic information is contained in the following components [26]:

$$C_0^0 \rightarrow R_{LCMS}, \quad (3.24)$$

$$\Re C_2^0 \rightarrow \frac{R_T}{R_{long}}, \quad (3.25)$$

$$\Re C_2^2 \rightarrow \frac{R_{out}}{R_{side}}, \quad (3.26)$$

where  $R_{LCMS} = \sqrt{(R_{out}^2 + R_{side}^2 + R_{long}^2)/3}$  and  $R_T = \sqrt{(R_{out}^2 + R_{side}^2)/2}$ . The  $C_0^0$  is sensitive to the overall size of a correlation function. The  $\Re C_2^0$  carries the information about the ratio of the transverse to the longitudinal radii, due to its  $\cos^2(\theta)$  weighting in  $Y_2^0$ . Finally, the component  $\Re C_2^2$  with its  $\cos^2(\phi)$  weighting encodes the ratio between outward and sideward radii. Thus, the spherical harmonics method allows to obtain and analyze full three-dimensional femtoscopic information from a correlation function [26].

### 3.3 Experimental approach

The correlation function is defined as a probability to observe two particles together divided by the product of probabilities to observe each of them separately (Eq. 3.18). In the experiment, this is achieved by dividing two distributions of relative momentum of pairs. The first one consists of particles coming from the same event while the second one is an equivalent distribution of pairs where each particle is taken from different collisions. In this way, one can investigate femtoscopic information as well as all other event-wide correlations. However, in the model calculations one has to include femtoscopic effects manually. In such a case, both distributions are generated from the same set of pairs, but the first one is filled with the  $|\Psi_{ab}|^2$  weights.

In order to calculate experimental-like correlation function, one uses the following approach. Two histograms, the *numerator*  $N$  and the *denominator*  $D$  are constructed with the particle pairs momenta, where particles are coming from the same event. These histograms can be one-dimensional (as a function of  $|\mathbf{q}|$ ), three-dimensional (as a function of three components of  $\mathbf{q}$  in LCMS) or a set of one-dimensional histograms representing components of the spherical harmonic decomposition of the distribution. The histogram  $D$  is filled for each pair with the weight 1.0 at a corresponding relative momentum  $\mathbf{q} = 2\mathbf{k}^*$ . The second one,  $N$  is filled with the same procedure, but the weight is calculated as  $|\Psi_{ab}(\mathbf{r}^*, \mathbf{k}^*)|^2$ . A division  $N/D$  gives the correlation function  $C$ . This process can be simply written as [26]:

$$C(\mathbf{k}^*) = \frac{N}{D} = \frac{\sum_{n_i \in D} \delta(\mathbf{k}^*_i - \mathbf{k}^*) |\Psi_{ab}(\mathbf{r}^*_i, \mathbf{k}^*_i)|^2}{\sum_{n_i \in D} \delta(\mathbf{k}^*_i - \mathbf{k}^*)} . \quad (3.27)$$

The  $D$  histogram represents the set of all particle pairs used in the calculations. The  $n_i$  is a pair with its relative momentum  $\mathbf{k}^*_i$  and relative separation  $\mathbf{r}^*_i$ . Explicit forms of wave function used in Eq. 3.27 are given by Eq. 3.6 (in the case of kaons and pions) and Eq. 3.7 (in the case of protons). Mathematically, the procedure of calculating the Eq. 3.27 is equivalent to a calculation of an integral in Eq. 3.19 through a Monte-Carlo method.

### 3.4 Scaling of femtoscopic radii

A particle interferometry formalism presented in the previous sections assumes that particle emitting source is static. However, this is not the case in heavy ion collisions at LHC. An existence of transverse radial and elliptic flows suggest that created system is dynamic. To address this issue, a concept of *lengths of homogeneity* was introduced. It is defined as:

$$\frac{|f(p, x + \lambda) - f(p, x)|}{f(p, x)} = 1 , \quad (3.28)$$

where  $\lambda$  is the homogeneity length, which can be interpreted as the distance where a relative change of the source Wigner function  $f$  becomes large. One can measure the lengths of homogeneity of a system using femtoscopic radii. This concept can be intuitively explained on a basis of hydrodynamic models. Every source element is emitting particles with a velocity being a combination of two components: a fluid cell velocity  $\beta_f$  (which is taken from the flow field  $u_\mu(\mathbf{x}^\mu)$ ) and thermal velocity  $\beta_{th}$  (which has random direction). These particles can combine into pairs of small relative momenta and become correlated. If two particles are emitted far away from each other ( $|\mathbf{x}_a - \mathbf{x}_b| > \lambda$ ), the flow field  $u_\mu$  in their point of emission might be very different. Hence, it will be impossible for them to have sufficiently small relative momenta to be in the region of interference effect. This effect is presented in Fig. 3.4. An increase of a correlation is visible for pairs with low relative momenta [8].

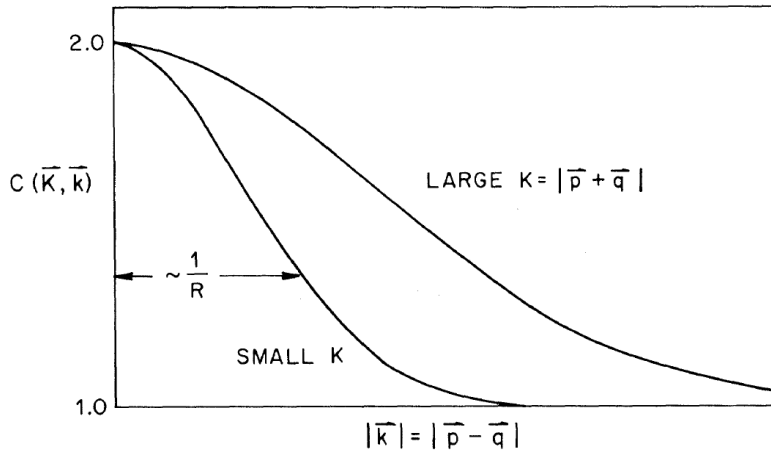


Figure 3.4: Correlation function width dependence on the total pair momentum. Pion pairs with a large total momentum have a wider correlation (smaller apparent source) [28].

### 3.4.1 Scaling in LCMS

Hydrodynamic calculations performed in LCMS show that femtoscopic radii in outward, sideward, and longitudinal directions show dependence on transverse mass  $m_T = \sqrt{k_T^2 + m^2}$ , where  $m$  is a mass of a particle [29]. Moreover, experimental results reveal that this scaling is observed for  $R_{LCMS}$  radii as well. This dependence can be expressed as follows:

$$R_i = \alpha m_T^{-\beta}, \quad (3.29)$$

where  $i$  subscript indicates that this equation applies to  $R_{out}$ ,  $R_{side}$  and  $R_{long}$  radii. The  $\beta$  exponent is approximately equal 0.5. However, in the case of strong

transversal expansion of the emitting source, the decrease of longitudinal interferometry radius can be more quick than  $m_T^{-0.5}$ . Hence, greater values of  $\beta > 0.5$  can be expected for longitudinal radii [29].

### 3.4.2 Scaling in PRF

In the collisions at the LHC energies, pions are the most abundant particles and their multiplicities are large enough to carry out three-dimensional analysis. However, for heavier particles, such as kaons and protons statistical limitations arise. Hence, it is often possible to measure only one-dimensional direction-averaged radius  $R_{inv}$  for those particles. The  $R_{inv}$  is then calculated in PRF. The transition from LCMS to PRF is a Lorentz boost in the direction of pair transverse momentum with velocity  $\beta_T = p_T/m_T$ . Hence only  $R_{out}$  changes:

$$R_{out}^* = \gamma_T R_{out}. \quad (3.30)$$

The Lorentz factor  $\gamma_T = m_T/m$  depends on the particle type. Therefore, for the lighter particles with the same  $m_T$ ,  $\gamma_T$  is much larger resulting in bigger growth of  $R_{out}$  and overall radius. This transformation to PRF breaks the scaling observed in LCMS radii.

This increase of radius in the outward direction induces overall source size growth and moreover the source distribution function becomes non-gaussian. In this case, the one-dimensional projection of a source function develops long-range tails and is much narrower in comparison to Gaussian distribution. This deformation is presented in Fig. 3.3. The influence of these effects can be expressed with an approximate formula:

$$R_{inv} = \sqrt{(R_{out}^2 \sqrt{\gamma_T} + R_{side}^2 + R_{long}^2)/3}. \quad (3.31)$$

Because the averaging of the radii is done in quadrature, one would have expected appearance of  $\gamma_T^2$  instead of  $\sqrt{\gamma_T}$  in this equation. However, the Monte-Carlo procedure shows that this is not the case and the actual growth is smaller than the naive expectation. Numerical simulations yield that this increase is best described with the  $\sqrt{\gamma_T}$  in the Eq. 3.31 [30].

Assuming that radii in all directions are equal  $R_{out} = R_{side} = R_{long}$ , Eq. 3.31 can be reverted using Eq. 3.17 to express relationship between LCMS and PRF overall radii [30]:

$$R_{LCMS} \approx R_{inv} \times [(\sqrt{\gamma_T} + 2)/3]^{-1/2}. \quad (3.32)$$

This approximate formula allows to restore common scaling of the divided radii not only when they are equal, but also when their differences are small (detailed explanation is given in Section 3.2.3).

This scaling recovery method in PRF can be used as a tool for the search of hydrodynamic collectivity between pions, kaons and protons in heavy ion collisions with the measurement of one-dimensional radius in PRF.

# Chapter 4

## Results

For the purpose of the femtoscopy analysis in this thesis, the THERMINATOR model was used to generate large number of events for eight different sets of initial conditions corresponding to the following centrality ranges: 0-5%, 0-10%, 10-20%, 20-30%, 30-40%, 40-50%, 50-60% and 60-70% for the Pb-Pb collisions at the centre of mass energy  $\sqrt{s_{NN}} = 2.76$  TeV. Software used in the process of calculating correlation functions is described in Appendix A, while plots presented in this chapter were generated using macros described in Appendix C.

### 4.1 Identical particles correlations

The correlation functions (three- and one-dimensional) were calculated separately for the following pairs of identical particles:  $\pi-\pi$ ,  $K-K$  and  $p-p$  for nine  $k_T$  bins (in GeV/c): 0.1-0.2, 0.2-0.3, 0.3-0.4, 0.4-0.5, 0.6-0.7, 0.7-0.8, 0.8-1.0 and 1.0-1.2. In the case of kaons,  $k_T$  ranges start from 0.3 while for protons from 0.4. For both of them the maximum value is 1.0. However, for the heavier particles  $k_T$  ranges were limited to maintain sufficient multiplicity to perform reliable calculations.

#### 4.1.1 Spherical harmonics components

The three-dimensional correlation function as a function of relative momentum  $q_{LCMS}$  was calculated in a form of components of the spherical harmonics series accordingly to Eq. 3.23. In the femtoscopy analysis of identical particles, the most important information is stored in the  $\Re C_0^0$ ,  $\Re C_2^0$  and  $\Re C_2^2$ , hence only these components were analyzed. Correlation functions obtained in this procedure were calculated for the pairs of pions, kaons and protons in the different centrality bins. They are presented in Fig. 4.1, 4.2 and 4.3.

Particular coefficients for pairs of identical bosons (pions and kaons) are shown in Fig. 4.1 and 4.2. The wave function symmetrization (Bose-Einstein statistics) causes the increase of correlation in the low relative momenta regime ( $q_{LCMS} < 0.06$  GeV/c or even  $q_{LCMS} < 0.12$  GeV/c for more peripheral

collisions). It is clearly visible in the  $\Re C_0^0$  component. The  $\Re C_0^0$  resembles one-dimensional correlation function in the sense that it encodes information about the overall source radius. The second coefficient  $\Re C_2^0$  differs from zero (is negative), which yields the information about the ratio  $R_T/R_{long}$ . The  $\Re C_2^2$  stores the information about  $R_{out}/R_{side}$  ratio and one can notice that is non-vanishing (is also negative).

Finally, the correlation function for a pair of identical fermions is presented in the Fig. 4.3. A wave function for a pair of protons is a composition of singlet (described by Bose-Einstein statistics) and triplet state (described by the Fermi-Dirac statistics - see Section 3.3). An influence of Fermi-Dirac statistics

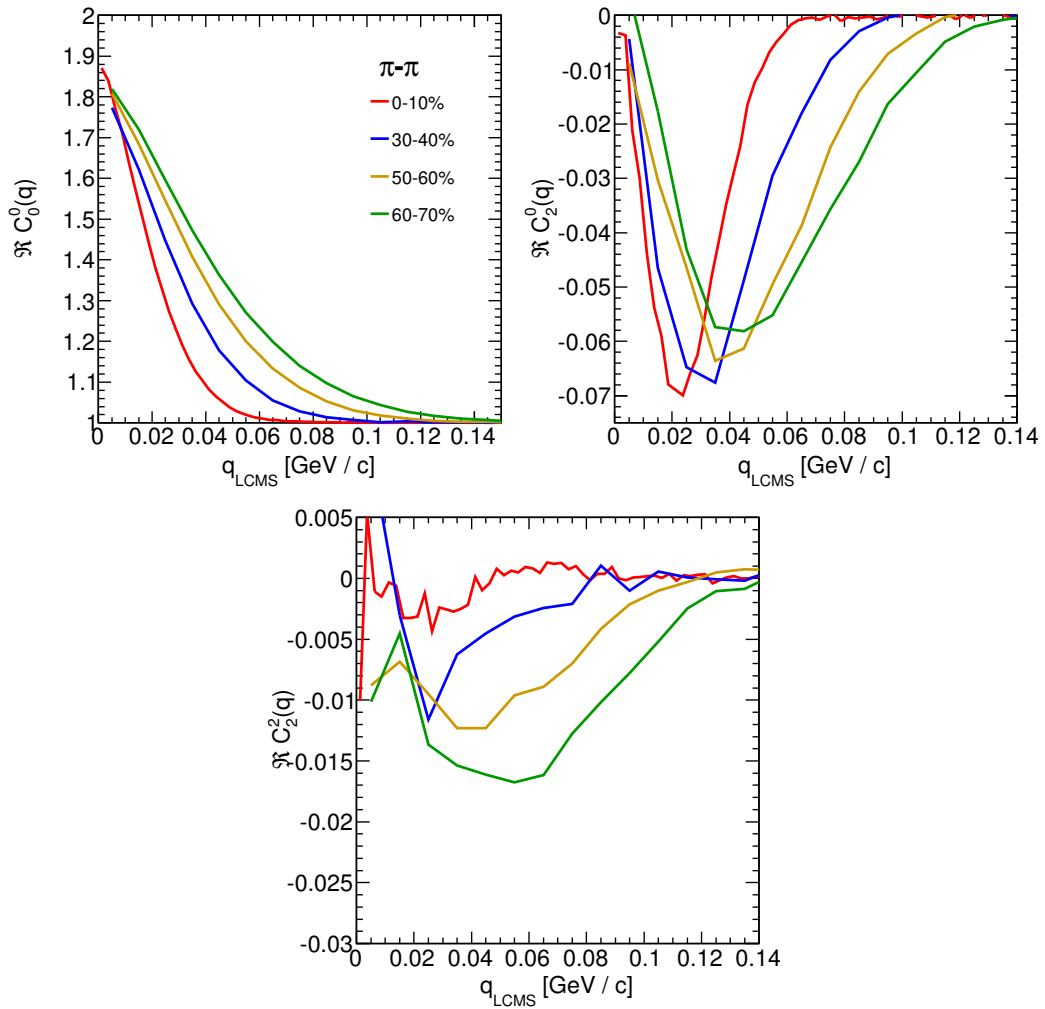


Figure 4.1: Spherical harmonics coefficients of the two-pion correlation function. From the top left:  $\Re C_0^0$ ,  $\Re C_2^0$  and  $\Re C_2^2$ . Only selected centrality bins are presented for increased readability.

has its effect in the decrease of a correlation down to 0.5 at low relative momentum ( $q_{LCMS} < 0.1 \text{ GeV/c}$  or  $q_{LCMS} < 0.15 \text{ GeV/c}$  for more peripheral collisions), which can be observed in  $\Re C_0^0$ . The  $\Re C_2^0$  and  $\Re C_2^2$  coefficients differ from zero and are becoming positive.

The common effect of the spherical harmonics form of a correlation function is the “mirroring” of the shape of the  $\Re C_0^0$  coefficient - when correlation function increases at low  $q_{LCMS}$ , the  $\Re C_2^0$  and  $\Re C_2^2$  are becoming negative and vice versa. This is quite different behaviour than in the case of correlations of non-identical particles, where the  $\Re C_2^0$  still behaves in the same manner, but  $\Re C_2^2$  has

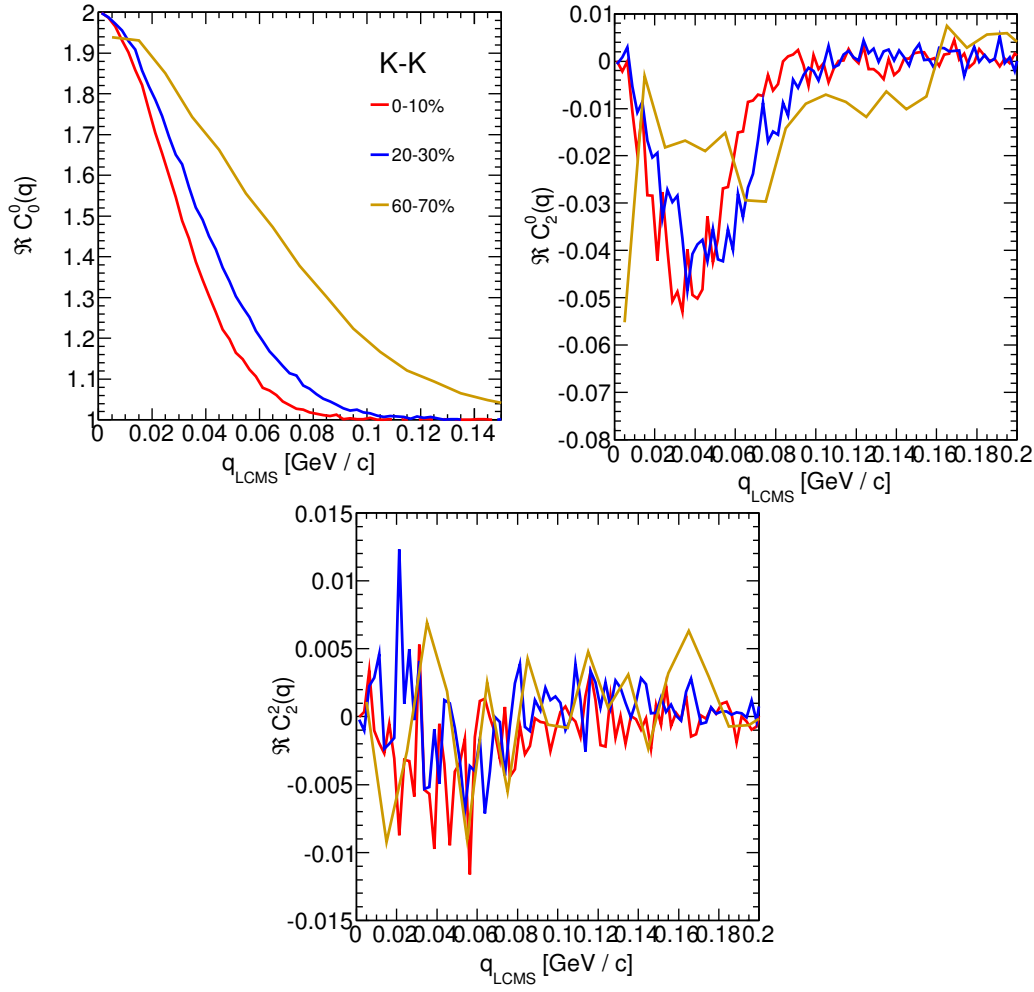


Figure 4.2: Spherical harmonics coefficients of the two-kaon correlation function. From the top left:  $\Re C_0^0$ ,  $\Re C_2^0$  and  $\Re C_2^2$ . Only selected centrality bins are presented for increased readability. The  $\Re C_2^2$  is noisy, but one can still notice that it differs from zero and is becoming negative.

the opposite sign to the  $\Re C_2^0$  [26].

In all cases, the correlation function gets wider with the peripherality of a collision i.e. the correlation function for most central collisions (0-10%) is much narrower than for the most peripheral ones (60-70%). This phenomenon is clearly visible in the  $\Re C_0^0$  coefficients. Moreover, other components are also affected by this effect, what is especially noticeable in the case of kaons and pions. However, the results for the protons are noisy, hence this effect is not clearly distinguishable.

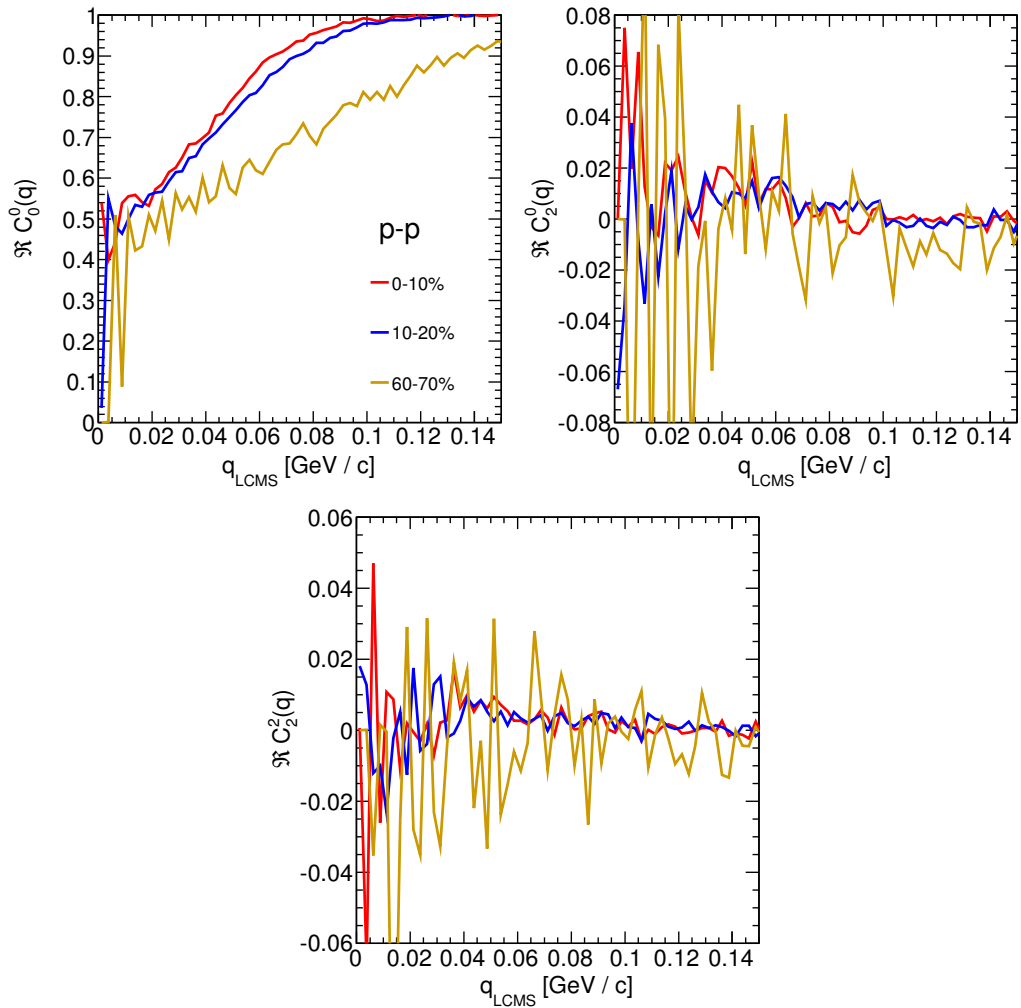


Figure 4.3: Spherical harmonics coefficients of the two-proton correlation function. From the top left:  $\Re C_0^0$ ,  $\Re C_2^0$  and  $\Re C_2^2$ . Only selected centrality bins are presented for increased readability. The  $\Re C_2^0$  and  $\Re C_2^2$  are noisy, but one can still notice, that they differ from zero and are becoming positive.

### 4.1.2 Centrality dependence of a correlation function

This centrality dependence is especially visible in one-dimensional correlation functions. This effect is presented in the Fig. 4.4 - the correlation functions for pions, kaons and protons are plotted for the same  $k_T$  range but different centrality bins. One can observe that the width of a function is smaller for the most central collisions. Hence, the femtoscopic radii (proportional to the inverse of width) are increasing with the centrality. Such increase can be explained by the fact that for the most central collisions, size of created system is larger than for the peripheral ones.

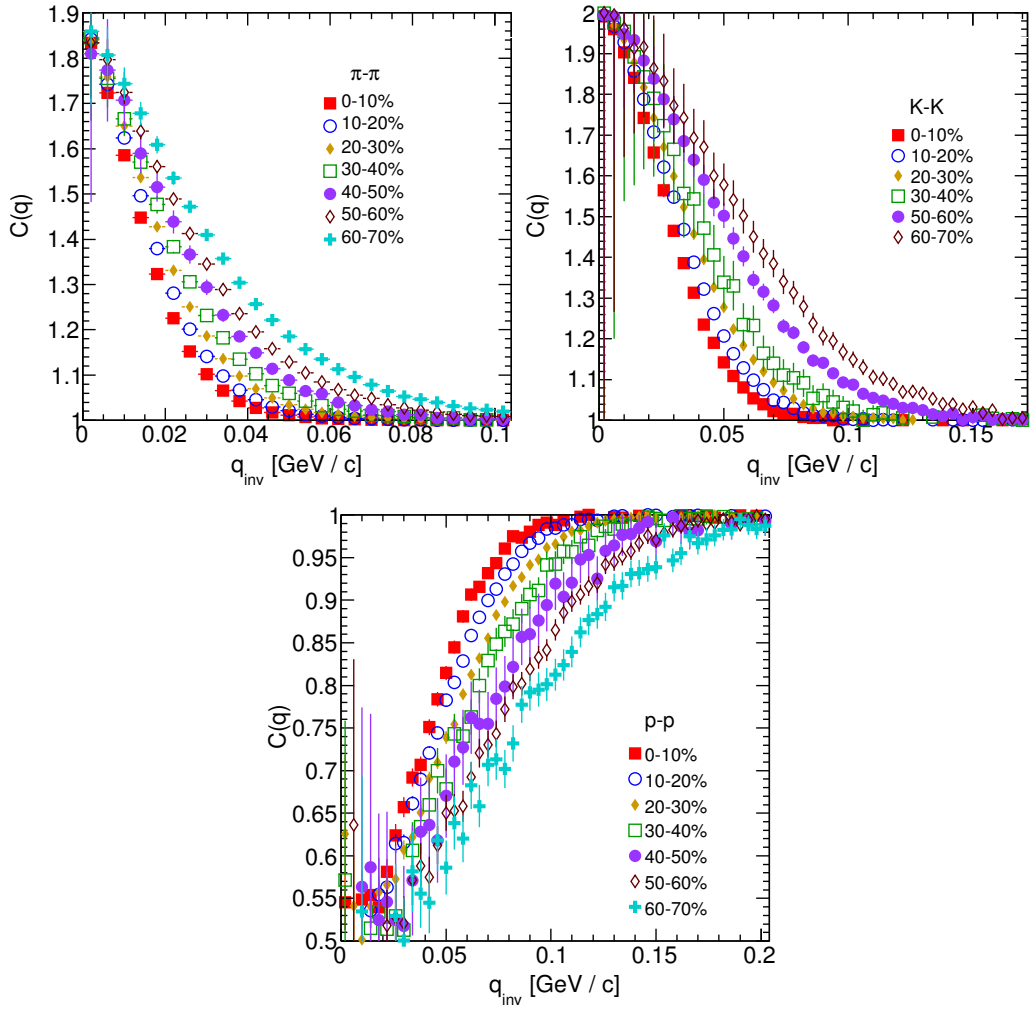


Figure 4.4: One-dimensional correlation function for pions (top left), kaons (top right) and protons (bottom) for different centralities.

### 4.1.3 $k_T$ dependence of a correlation function

In Fig. 4.5 one-dimensional correlation functions are presented for pions, kaons and protons for the same centrality bin but different  $k_T$  ranges. For all particles types, one can notice appearance of the same trend: the width of a correlation function increases and the femtoscopic radius decreases with the increase of the total transverse momentum of a pair. The plots in Fig. 4.5 were zoomed in to show the influence of  $k_T$ .

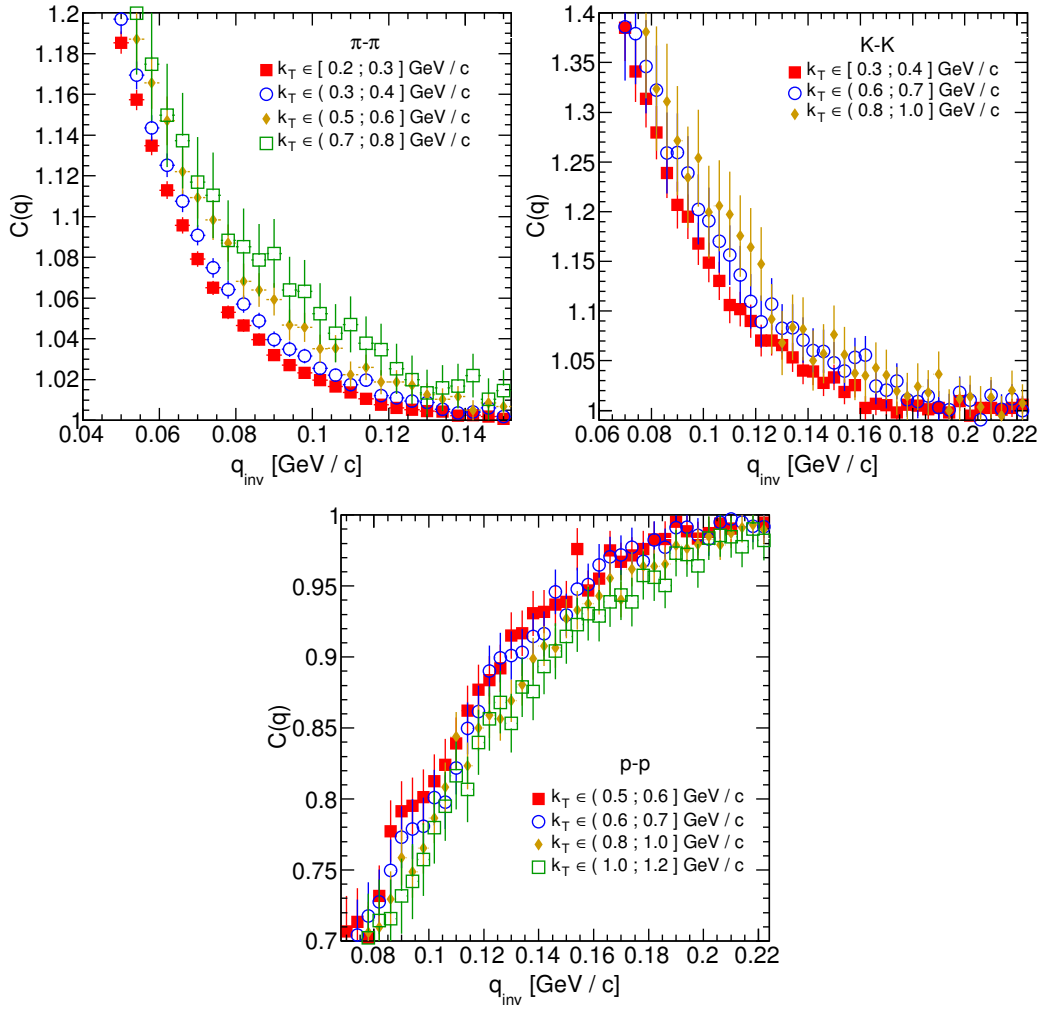


Figure 4.5: One-dimensional correlation functions for pions, kaons and protons in the same centrality bin and different  $k_T$  ranges. The plot was zoomed in to the region which illustrates the  $k_T$  dependence in the best way. Only selected calculated ranges are presented for a better readability.

## 4.2 Results of the fitting procedure

In order to perform a quantitative analysis of a wide range of correlation functions, the fitting procedure was carried out. To each of the one-dimensional correlation functions its analytical formula given by Eq. 3.20 was fitted, which yields the  $\lambda$  parameter and  $R_{inv}$ . Fig. 4.6 presents sample correlation function calculated for pairs of protons with the fit of the analytical formula. In turn, to extract  $R_{out}$ ,  $R_{side}$ ,  $R_{long}$  as well as  $\lambda$ , the fitting of Eq. 3.21 to the three-dimensional correlation functions was conducted. This fitting process gives besides the best fit parameters also their statistical uncertainties.

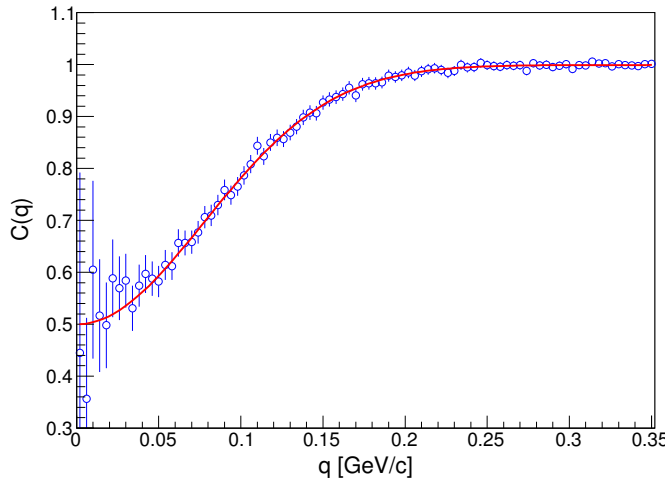


Figure 4.6: One-dimensional proton-proton correlation function. The red line represents analytical formula fit.

The main goal of this analysis is a verification of a common transverse mass scaling for different particles types. To deal with this task, radii extracted in the previous step were plotted as a function of a transverse mass  $m_T = \sqrt{k_T^2 + m^2}$ . Finally, to test the scaling accuracy, the following power-law was fitted to the radii for each of the centrality bins:

$$R_x = \alpha m_T^{-\beta}, \quad (4.1)$$

where  $\alpha$  and  $\beta$  are free parameters. The software used in this fitting process is described in Appendix B.

### 4.2.1 The three-dimensional femtoscopic radii scaling

The femtoscopic radii in the outward, sideward and longitudinal directions for the analysis of two-pion correlation functions in LCMS are

presented in Fig. 4.7. The dashed lines represent fits of the-power law. One can notice that the power-law describes well data points with a 5% accuracy. The  $\beta$  fit parameter for the outward direction is in the order of 0.45. For the sideward direction, this parameter has the similar value, but it is lower for the most peripheral collisions. In the case of the longitudinal direction, the  $\beta$  has greater value, up to 0.75. Moreover, in Fig. 4.7, the results for the top 5% central collisions (star-shaped markers) are also compared with experimental data from ALICE [31]. One can notice that the experimental results are consistent with the ones coming from the model predictions.

Femtoscopic radii coming from the kaon calculations are presented in Fig. 4.8. The  $R_{out}$ ,  $R_{side}$  and  $R_{long}$  also fall with the power-law within the 5% accuracy. The  $\beta$  parameter was larger in the case of kaons: 0.59 in outward, 0.54 in the sideward and 0.86 for longitudinal directions.

The results for two-proton analysis are shown in Fig. 4.9. The result of fitting Eq. 4.1 to the data gives the information that protons also follow the  $m_T$  scaling with 5% accuracy. The  $\beta$  parameter values were even bigger for the outward (0.58), sideward (0.61) and longitudinal (1.09) directions than for the other particle types.

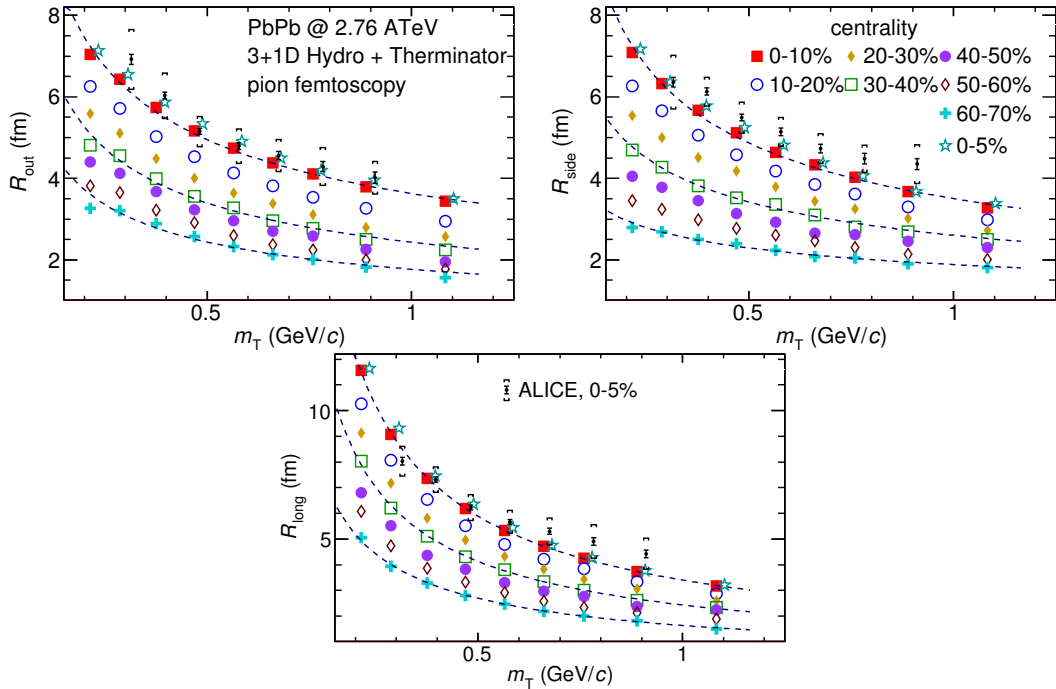


Figure 4.7: Femtoscopic radii in LCMS coming from two-pion correlation functions for all centrality bins as a function of  $m_T$ . The dashed lines are power-law fits. The most central collisions (0-5%) are compared to the results from ALICE [31]. The two datasets are shifted to the right for a better visibility [30].

The results for the pions, kaons and protons together as a function of  $m_T$  are presented in Fig. 4.10. Considering differences in the  $\beta$  value in the fits for different particles, one can suspect that there is no common scaling between different kinds of particles. However, when all of the results are shown on the same plot, they are aligning on the common curve and the scaling is well preserved. The scaling accuracy is 3%, 5% and 4% for the 0-10%, 20-30% and 60-70% centrality bins for the outward direction. In the case of the sideward radii the scaling is better, with average deviations 2%, 2% and 3% respectively. Finally, the accuracy for the longitudinal direction is 6%, 5% and 3% for these three centralities. The  $\beta$  parameter for the outward direction is close to 0.42 in all cases. For the sideward direction it varies from 0.28 to 0.47 and is bigger for more central collisions. Regarding longitudinal radii, the exponent is bigger than the other two:  $\beta \in [0.62; 0.72]$ . Considering all results, the plotted radii are following the common power-law scaling within the 5% accuracy for all directions, centralities and particle types.

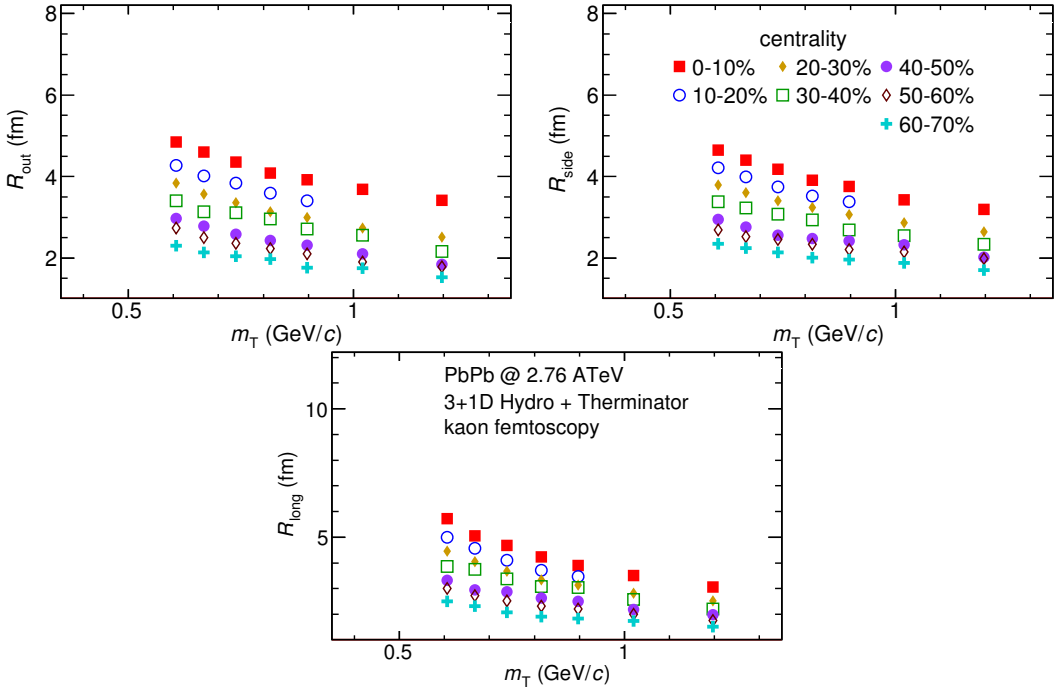


Figure 4.8: Femtoscopic radii extracted from two-kaon correlation functions for different centrality bins as a function of  $m_T$ . [30].

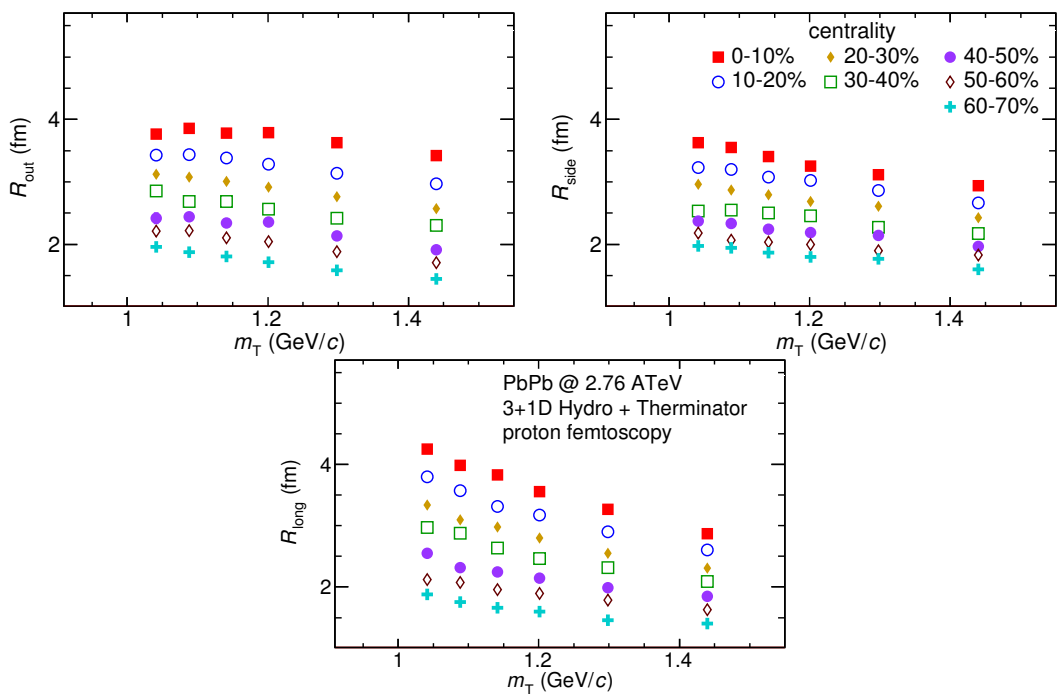


Figure 4.9: Femtoscopic radii extracted from two-proton correlation functions for different centrality bins as a function of  $m_T$ . [30].

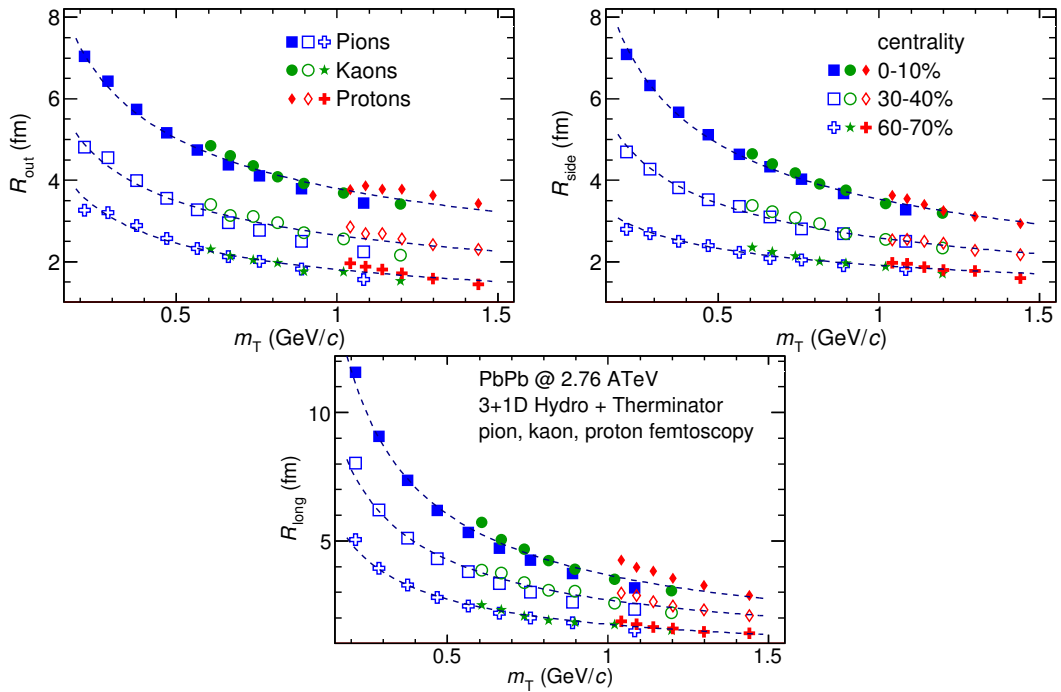


Figure 4.10: The results from the calculations for pions, kaons and protons for the three centralities presented on the same plot. One can notice that radii for particular centralities and different particle types follow the common power-law scaling. [30].

### 4.2.2 Scaling of one-dimensional radii

To the one-dimensional correlation function, the analytical formula in PRF given by Eq. 3.20 was fitted. The results obtained from these fits are presented in the upper left plot in Fig. 4.11. One can notice that there is no common scaling of  $R_{inv}$  for different kind of particles. The radii for pions, kaons and protons in the outward direction presented in Fig. 4.10 are similar for the same  $m_T$ . However, during the transition from LCMS to PRF the  $R_{out}$  radius grows as follows:

$$R_{out}^* = \gamma_T R_{out}, \quad (4.2)$$

where  $\gamma_T = m_T/m$ . For the lighter particles, the  $\gamma_T$  is much larger, hence the bigger growth of the  $R_{out}$  and the overall radius. This is visible in Fig. 4.11 (top left), where the radii in PRF for the lighter particles are bigger than for the heavier ones in the case of the same  $m_T$  range.

In Fig. 4.10, the scaling is visible in the outward, sideward and longitudinal directions. Hence, one can expect an appearance of such scaling in a direction-averaged radius calculated in LCMS. This radius is presented in the Fig. 4.11 (bottom) and indeed the  $R_{LCMS}$  exhibits power-law scaling with  $m_T$ .

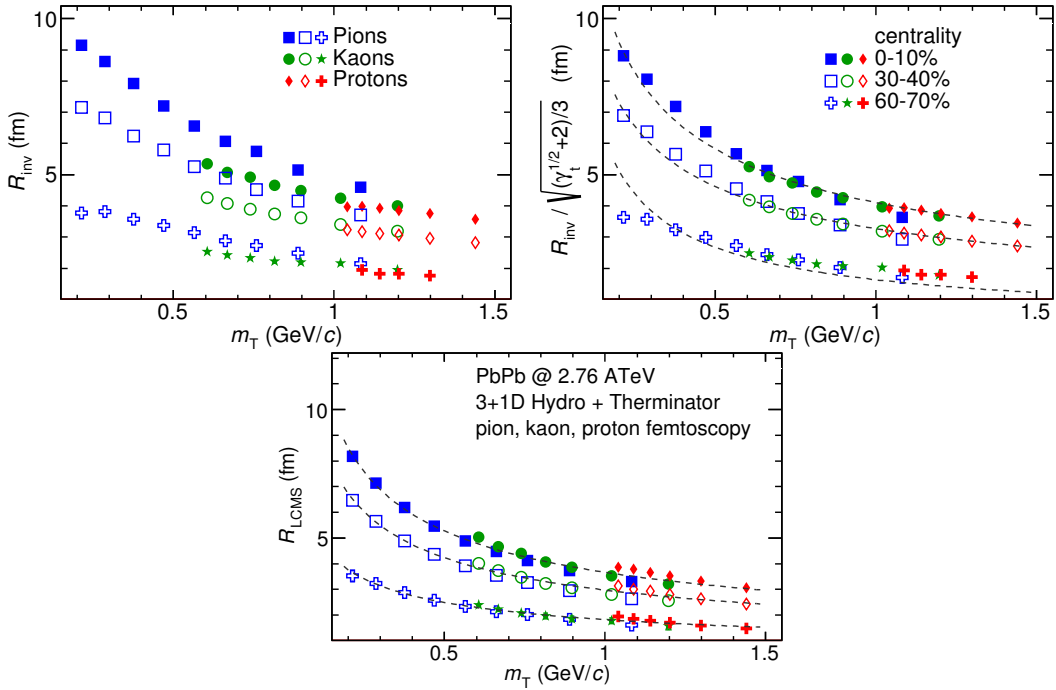


Figure 4.11: Top left: one-dimensional radius for pions, kaons and protons calculated in PRF. Top right: the  $R_{inv}$  scaled by the proposed factor. Bottom: averaged one-dimensional radius in LCMS for pions, kaons and protons. Only three centrality bins are shown for a better readability [30].

One can try to account the effect of an increase of the radii in the outward direction by using the appropriate scaling factor. In Fig. 4.11 (top right), femtoscopic radii in LCMS are divided by the proposed factor (described in Section 3.4.2):

$$f = \sqrt{(\sqrt{\gamma_T} + 2)/3} . \quad (4.3)$$

The radii for pions, kaons and protons in PRF after the division by  $f$  are following the power-law with the accuracy of 10%.

### 4.3 Discussion of the results

The femtoscopic radii obtained from the three-dimensional correlation function fitting exhibit the  $m_T$  dependence described by the power-law (Eq. 4.1). This scaling is preserved quite well with accuracy  $< 10\%$ . Observation of  $m_T$  dependence of femtoscopic radii is a strong signal of the collective behaviour of a particle-emitting source created in the collision. The data used in the analysis was coming from the hydrodynamic model, hence one can indeed expect the appearance of this scaling. The results for pion femtoscopy from the ALICE at LHC are consistent with the data from analysis performed in this thesis (Fig. 4.7). This is a confirmation of applicability of hydrodynamic models in a description of evolution of a quark-gluon plasma.

The  $\beta$  parameter calculated in the fitting of the power-law to the femtoscopic radii is of the order of 0.5 in the case of the radii in the transverse plane. This value is consistent with the hydrodynamic predictions. On the other side, for longitudinal radii the exponent is bigger (greater than 0.7), which is an indication of a strong transversal expansion in the system [29].

A scaling described above is visible in LCMS. However due to limited statistics, analysis in this reference frame is not always possible. In such a case, one performs calculations in the PRF where the scaling is not observed - it has a trivial kinematic origin. A transition from PRF to LCMS causes growth of the radius in the outward direction and the common power-law scaling for various particles breaks due to differences in the  $\gamma_T(m_T)$  for different particle types. However, one can try to deal with the radius growth and restore the scaling through dividing the radii  $R_{inv}$  by an approximate factor  $\sqrt{(\sqrt{\gamma_T} + 2)/3}$ . The scaled  $R_{inv}$  are following the power-law and could be used as a verification of hydrodynamic behaviour in the investigated particle source.

The hadronic evolution and freeze-out in THERMINATOR is followed by the resonance propagation and decay phase. A good agreement of the results with the power-law show that the inclusion of the resonances does not break the  $m_T$  scaling. However, recent calculations, which include also hadron rescattering phase, indicate that the scaling between pions and kaons is broken at the LHC [32]. Thus, the results of this work suggest that the scaling breaks at the hadron rescattering phase [30].

# Conclusions

This thesis presents the results of the two-particle femtoscopy for different particle kinds produced in Pb-Pb collisions at the centre of mass energy [ $\sqrt{s_{NN}} = 2.76 \text{ TeV}$ ]. The analysed data was generated by the THERMINATOR model using hypersurfaces from (3+1)-dimensional hydrodynamic calculations.

The momentum correlations were studied for three types of particle pairs: pions, kaons and protons. The data was analyzed for eight sets of initial conditions corresponding to the following centrality ranges: 0-5%, 0-10%, 10-20%, 20-30%, 30-40%, 40-50%, 50-60% and 60-70%. The correlation functions were calculated for nine  $k_T$  bins from 0.1 GeV/c to 1.2 GeV/c. The calculations were performed using spherical harmonics decomposition of a three-dimensional correlation function. Using this approach, one can obtain full three-dimensional information about the source size using only the three coefficients:  $\Re C_0^0$ ,  $\Re C_2^0$  and  $\Re C_2^2$ . To perform further quantitative analysis, the femtoscopic radii were extracted through fitting procedure.

The calculated correlation functions show expected increase of a correlation at low relative momenta in the case of identical bosons (pions and kaons) and decrease for identical fermions (protons). This effect is especially visible in the first spherical harmonic coefficient  $\Re C_0^0$ . The other two components  $\Re C_2^0$  and  $\Re C_2^2$  are non-vanishing and provide information about the ratios of radii in the outward, sideward and longitudinal directions.

An increase of the width of a correlation function with the peripherality of a collision and also with the pair transverse momentum  $k_T$  is observed for pions, kaons and protons. This increase of femtoscopic radii (proportional to the inverse of width) with  $k_T$  is related with the  $m_T$  scaling coming from the hydrodynamics.

Hydrodynamic equations are predicting the appearance of the common scaling of femtoscopic radii for different kinds of particles with  $m_T^{-0.5}$  in LCMS. In the results of this work, a common scaling for different particle types is observed in LCMS in the outward, sideward and longitudinal directions. The direction-averaged radius  $R_{LCMS}$  also shows this power-law behaviour. The fitting of a power-law  $\alpha m_T^{-\beta}$  to the femtoscopic radii yielded the information that the  $\beta$  exponent for the outward and sideward directions is of the order of 0.5, which is consistent with the hydrodynamic predictions. For the longitudinal direction, the  $\beta$  is bigger ( $>0.7$ ) than in the other ones, which is an indication of a strong longitudinal flow. Femtoscopic radii in LCMS are following the power-law scaling

with the accuracy  $< 5\%$  for pions and kaons, and  $< 10\%$  for protons.

In the case of the one-dimensional radii  $R_{inv}$  calculated in PRF, no common scaling is observed. This is a consequence of a transition from LCMS to PRF, which causes the growth of radius in the outward direction and breaks the scaling for different particles. However, one can try to correct the influence of the  $R_{out}$  growth with an approximate factor  $\sqrt{(\sqrt{\gamma T} + 2)/3}$ . After the division of the  $R_{inv}$  by the proposed factor, the scaling is restored with an accuracy  $< 10\%$ . In this way, the experimentally simpler measure of the one-dimensional radii can be used as a probe for the hydrodynamic collectivity.

The THERMINATOR model includes hydrodynamic expansion, statistical hadronization, resonance propagation and decay afterwards. The  $m_T$  scaling is predicted from the pure hydrodynamic calculations. However, this study shows that influence of the resonances on this scaling is less than 10%.

## Appendix A

# Scripts for correlation function calculations

### A.1 Events generation

In order to perform analysis with sufficient statistics, a big number of events is required. To handle this task, a computer cluster at Faculty of Physics at Warsaw University of Technology was used. This cluster consists of 20 nodes with the following hardware configuration: Intel® Core™ 2 Quad CPU Q6600 @ 2.40GHz, 8GB RAM with Scientific Linux 5.8. The communication between nodes is realized by the TORQUE Resource Manager [33]. To control the process of launching multiple event generators and collecting the data, the following scripts were written using Bash scripting language:

**skynet.sh** This is a script in a form of a batch job for TORQUE. It simply launches multiple THERMINATOR processes in the same working directory with the separate output folders for each job. This solution has two advantages: saves space and computation time. First of all, a single freeze-out hypersurface file has size about 230 MB. This approach allows to avoid time- and space-consuming copying of the whole THERMINATOR directory before running the application. Thus, in the case of running 20 instances of this generator, it makes significant difference. The second advantage is a possibility to share files containing information about particles' multiplicities and maximum integrands between generator processes (more detailed description is presented in Section 2.3). One can simply execute this batch job using the following command:

```
qsub -q long -t 0-19 skynet.sh -v dir=th_5.7,events=6000
```

It adds 20 event generators (with task ids from 0 to 19) to the queue, sets the THERMINATOR directory as `th_5.7` and a number of simulated events to 6000 for each process. This command should be executed in the directory one level higher than `th_5.7` folder.

**merge\_events.sh** After the generation process, one has to merge calculated events into one directory. This task requires renaming of a large number of THERMINATOR event files. Each event generator job produces files named with a certain pattern, starting from event000.root with increasing number. In order to move the event files and preserve continuity in the numbering, a simple script was written. An example of use:

```
find /data/source -iname "event*.root" -type f \
| merge_events.sh
```

This command will find all the event files in the folder /data/source, move and rename them accordingly to the enumeration of events in the current working directory.

Sources of these two scripts are available on-line at <https://github.com/carbolymer/msc/tree/master/alix>.

## A.2 Calculations of experimental-like correlation functions

Correlation functions utilized in this analysis were calculated using *tpi* software written by Adam Kisiel and designed for reading event files from THERMINATOR. It uses ROOT library for calculations and storage of the data. This application provides functionality of calculation of one-dimensional correlation functions in PRF, three-dimensional one in LCMS and its spherical harmonics decomposition (see Section 3.2.5). The exact numerical procedure of computation of a correlation function is presented in Section 3.3. *tpi* allows to perform calculations with the following options:

- Pair type - there are pion-pion, kaon-kaon, proton-proton and many more pairs available (including ones consisting of non-identical particles)
- Multiple  $k_T$  subranges from 0.21 to 1.2 GeV/c
- Possibility to include Coulomb interaction
- Number of events to mix
- Maximum freeze-out time
- Choice of method of background calculation in correlation function (mixing events or using particles from the same event)

This program generates results in the \*.root files format in a form of histograms. Output file contains numerators, denominators and correlation functions from one-dimensional and three-dimensional analyses. Moreover, the spherical harmonics series coefficients up to  $l = 3$  with signal and background histograms are stored.

# Appendix B

# Fitting utilities

Procedure of fitting analytical formulas to experimental-like correlation functions was performed using custom software written in C++ and Bash. This application utilizes MINUIT [34] package built in the ROOT library.

The source of fitting software is available on-line at <https://github.com/carbolymer/msc/tree/master/fitting>.

## B.1 Minuit package

The MINUIT is a physics analysis tool for function minimization written in Fortran programming language. This tool was designed for statistical analysis and it is working on  $\chi^2$  or log-likelihood functions to compute the best-fit parameter values and uncertainties, including correlations between parameters. It is implemented in ROOT environment as `TMinuit` class, which provides interface to the minimization tool. The analysis performed in this work uses MINUIT with the Migrad minimization method. The Migrad minimizer is the best one embedded in Minuit. It is a variable-metric method with inexact line search, a stable metric updating scheme, and checks for positive-definiteness [34].

## B.2 Fitting software

Fitting application provides tools for extraction of femtoscopic radii from correlation functions for identical particles. It also provides a macro for generating plots with radii as a function of transverse mass and fitting power-law  $\alpha m_T^{-\beta}$  to the results.

### B.2.1 Input parameters

The application reads the output files from the `tpi` program and extracts from them one-dimensional and three-dimensional correlation functions. The latter ones are in a form of spherical harmonics series coefficients.

The program gives a possibility to set fit parameters for certain centrality bins, pair types and  $k_T$  ranges. Configuration files (\*.conf) are located inside the application's folder in the `data/` directory. Files with the names beginning with `fitsh` contain parameters for three-dimensional fits, while `fit1d` prefix indicates settings for one-dimensional ones. In principle, names of the parameter files are following this pattern: `{fit type}.{centrality}.{pair type}.{kT range beginning}.conf`, for example: `fit1d.b3.1.pp.0.6.conf`. To set parameters for all fits of the same kind of particles, one has to create a file with the following name: `{fit type}.{pair type}.conf`. For example, `fitsh.kk.conf` file contains initial parameters for all fits for kaon pairs. Similarly, one can set fit parameters for pions (`pipi`) and protons correlation functions (`pp`) using corresponding letters in place of `kk` in the name of the file.

An example content of configuration file for one-dimensional fit (**fit1d**) is presented below:

1.0	L	normalization
1.0	L	$\lambda$
4.0	L	$R_{inv}$
0.0	F	not used

The *F* letter after the parameter indicates fixed value (will not change during fitting process), whereas the *L* parameter tells that this value will be modified.

An example configuration file for three-dimensional fit (**fitsh**):

0.0 F 0.0 0.0	not used
0.0 F 0.0 0.0	not used
IdLCY1m	correlation function numerator name
0.0075	beginning of the fitting range ( $q$ in GeV/c)
0.2	end of the fitting range ( $q$ in GeV/c)
0	not used

This file contains extra columns to specify the allowed range for the value of a fit parameter. The minimum of the range is determined by the value in the 3rd column, while the 4th column contains its maximum.

### B.2.2 Output format

The application during calculations creates subdirectories for each centrality inside the `data/` directory. For each pair type and each of the following variables  $R_{inv}$ ,  $R_{out}$ ,  $R_{side}$ ,  $R_{long}$ ,  $\lambda$  and  $R_{LCMS}$ , the output files `*.out` with four columns are created. First column is the beginning of the  $k_T$  range, while the second one is its end, third column contains result of the fit and the last one stores uncertainty of this value. In addition, plots (in the png format) of the correlation functions for each pair type and  $k_T$  bin are generated inside subdirectories.

Files `filelist.{pair type}.in` include list of input `*.root` files with processed correlation functions.

### B.2.3 Compilation

This utility requires ROOT framework and libboost-regex-dev library. Compilation can be performed using `make` command inside application's directory.

### B.2.4 Usage

#### Fitting process

In order to start the fitting process, one should execute the following command:

```
./run.sh /path/to/the/tpi/output centrality
```

The `/path/to/the/tpi/output` parameter is a location of tpi output files and `centrality` is a name of a directory, where the fitting results will be stored.

## Plotting

In order to plot femtoscopic radii and perform fitting of power law, one has to use the following command:

```
make plots
```

Plots will be generated in the output directory.

# Appendix C

## Plotting scripts

### C.1 Correlation functions plots

Plots containing correlation functions were generated using two ROOT macros written in C++.

The first one, **cf1DAllCentralities.C** generates two plots with one-dimensional correlation functions. One of them presents  $k_T$  dependence of a correlation function (saved in the *cfvskt.eps* file), while the other one shows influence of centrality on a correlation function (saved in the *cfvsctr.eps* file). In order to generate plots, one has to set in the line 9 the path to the folder including subdirectories with correlation functions files. One can produce eps files, using the following command:

```
root -l -b -q cf1DAllCentralities.C
```

*cfvskt.eps* and *cfvsctr.eps* files will be generated in the current working directory.

The second macro, **cf3DAllCentralities.C** produces plots with spherical harmonics coefficients for pions (*cf3dpi.eps*), kaons (*cf3dk.eps*) and protons (*cf3dp.eps*). This script has similar structure to the previous one. Like in the previous case, one also has to set the proper path in the line 18. To execute this macro, one can use this command:

```
root -l -b -q cf3DAllCentralities.C
```

As a result, the three files with the output plots will be generated in the current working directory.

The sources of these plotting macros are available on-line at <https://github.com/carbolymer/msc/tree/develop/fitting/macros>.

### C.2 Plots with femtoscopic radii

Femtoscopic radii plots can be generated using fitting tool described in Appendix B. To do so, one has to invoke the following command:

```
make plots
```

This command executes ROOT macro *src/plotter.C* which generates all plots for

every centrality automatically. This script for every pair type,  $k_T$  and centrality bin reads the femtoscopic radii and calculates the transverse mass. Afterwards, to all of the femtoscopic radii as a function of transverse mass, the following formula is fitted:  $R_x = \alpha m_T^{-\beta}$ . It should be noted, that the fitting is performed to the radii of pions, kaons and protons together. As a result of this process, plot with the femtoscopic radii in the outward, sideward, and longitudinal direction as well as overall radii is generated for every centrality. Moreover, the comparison between different centralities in PRF divided by the scaling factor (see Section 3.4) and the  $R_{LCMS}$  are also plotted.

# Bibliography

- [1] Standard Model of Elementary Particles - Wikipedia, the free encyclopedia [http://en.wikipedia.org/wiki/Standard\\_Model](http://en.wikipedia.org/wiki/Standard_Model).
- [2] R. Aaij et al. (LHCb Collaboration). Observation of the resonant character of the  $z(4430)^-$  state. *Phys. Rev. Lett.*, 112:222002, Jun 2014.
- [3] Donald H. Perkins. *Introduction to High Energy Physics*. Cambridge University Press, fourth edition, 2000. Cambridge Books Online.
- [4] G. Odyniec. *Phase Diagram of Quantum Chromo-Dynamics* - course at Faculty of Physics, Warsaw University of Technology, Jun 2012.
- [5] J. Beringer et al. (Particle Data Group). The Review of Particle Physics. *Phys. Rev.*, D86:010001, 2012.
- [6] Z. Fodor and S.D. Katz. The Phase diagram of quantum chromodynamics. 2009.
- [7] F. Karsch. Lattice results on QCD thermodynamics. *Nuclear Physics A*, 698(1-4):199 – 208, 2002.
- [8] Adam Kisiel. *Studies of non-identical meson-meson correlations at low relative velocities in relativistic heavy-ion collisions registered in the STAR experiment*. PhD thesis, Warsaw University of Technology, Aug 2004.
- [9] J. Bartke. *Relativistic Heavy Ion Physics*. World Scientific Pub., 2009.
- [10] W. Florkowski. *Phenomenology of Ultra-Relativistic Heavy-Ion Collisions*. World Scientific, 2010.
- [11] Science Grid This Week, October 25, 2006 - Probing the Perfect Liquid with the STAR Grid [http://www.interactions.org/sgtw/2006/1025/star\\_grid\\_more.html](http://www.interactions.org/sgtw/2006/1025/star_grid_more.html).
- [12] K. Grebieszkow. Fizyka zderzeń ciężkich jonów, <http://www.if.pw.edu.pl/~kperl/HIP/hip.html>.
- [13] Ulrich W. Heinz. From SPS to RHIC: Maurice and the CERN heavy-ion programme. *Phys. Scripta*, 78:028005, 2008.

- [14] J. Adams et al. Identified particle distributions in pp and Au+Au collisions at  $s_{\text{NN}}^{**}(1/2) = 200 \text{ GeV}$ . *Phys.Rev.Lett.*, 92:112301, 2004.
- [15] G. David, R. Rapp, and Z. Xu. Electromagnetic Probes at RHIC-II. *Phys.Rept.*, 462:176–217, 2008.
- [16] A. Marin et al. Dilepton measurements with CERES. *PoS*, CPOD07:034, 2007.
- [17] J. Adams et al. Experimental and theoretical challenges in the search for the quark gluon plasma: The STAR Collaboration’s critical assessment of the evidence from RHIC collisions. *Nucl.Phys.*, A757:102–183, 2005.
- [18] Adam Kisiel, Tomasz Taluc, Wojciech Broniowski, and Wojciech Florkowski. THERMINATOR: THERMal heavy-IoN generATOR. *Comput.Phys.Commun.*, 174:669–687, 2006.
- [19] Mikolaj Chojnacki, Adam Kisiel, Wojciech Florkowski, and Wojciech Broiniowski. THERMINATOR 2: THERMal heavy IoN generATOR 2. *Comput.Phys.Commun.*, 183:746–773, 2012.
- [20] ROOT - A Data Analysis Framework <http://root.cern.ch/drupal/>.
- [21] I. et al (BRAHMS Collaboration) Bearden. Charged meson rapidity distributions in central Au + Au collisions at  $\sqrt{s_{\text{NN}}} = 200 \text{ GeV}$ . *Phys. Rev. Lett.*, 94:162301, Apr 2005.
- [22] W. Israel and J.M. Stewart. Transient relativistic thermodynamics and kinetic theory. *Annals of Physics*, 118(2):341 – 372, 1979.
- [23] Piotr Bożek. Flow and interferometry in (3 + 1)-dimensional viscous hydrodynamics. *Phys. Rev. C*, 85:034901, Mar 2012.
- [24] K. Kovtun, P. D. T. Son, and A. O. Starinets. Viscosity in strongly interacting quantum field theories from black hole physics. *Phys. Rev. Lett.*, 94:111601, Mar 2005.
- [25] Fred Cooper and Graham Frye. Single-particle distribution in the hydrodynamic and statistical thermodynamic models of multiparticle production. *Phys. Rev. D*, 10:186–189, Jul 1974.
- [26] Adam Kisiel. Nonidentical-particle femtoscopy at  $\sqrt{s_{\text{NN}}} = 200 \text{ GeV}$  in hydrodynamics with statistical hadronization. *Phys. Rev. C*, 81:064906, Jun 2010.
- [27] Adam Kisiel and David A. Brown. Efficient and robust calculation of femtoscopic correlation functions in spherical harmonics directly from the raw pairs measured in heavy-ion collisions. *Phys.Rev.*, C80:064911, 2009.

- [28] S. Pratt. Pion Interferometry for Exploding Sources. *Phys.Rev.Lett.*, 53:1219–1221, 1984.
- [29] S.V. Akkelin and Yu.M. Sinyukov. The HBT-interferometry of expanding inhomogeneous sources. *Z.Phys.*, C72:501–507, 1996.
- [30] A. Kisiel, M. Galazyn, and P. Bozek. Pion, kaon, and proton femtoscopy in Pb–Pb collisions at  $\sqrt{s_{NN}}=2.76$  TeV modeled in 3+1D hydrodynamics. 2014.
- [31] K. Aamodt et al. Two-pion Bose-Einstein correlations in central Pb-Pb collisions at  $\sqrt{s_{NN}} = 2.76$  TeV. *Phys.Lett.*, B696:328–337, 2011.
- [32] V.M. Shapoval, P. Braun-Munzinger, Iu.A. Karpenko, and Yu.M. Sinyukov. Femtoscopy correlations of kaons in  $Pb + Pb$  collisions at LHC within hydrokinetic model. 2014.
- [33] TORQUE Resource Manager - An open source resource manager providing control over batch jobs and distributed compute nodes <http://www.adaptivecomputing.com/products/open-source/torque/>.
- [34] MINUIT - Function Minimization and Error Analysis <http://wwwasdoc.web.cern.ch/wwwasdoc/minuit/minmain.html>.

# List of Figures

1.1	The Standard Model of elementary particles [1]. . . . .	3
1.2	A string breaking and a creation of a new quark-anti-quark pair [4]. . . . .	5
1.3	The coupling parameter $\alpha_s$ dependence on four-momentum transfer $Q^2$ [5]. . . . .	6
1.4	The QCD potential for a quark-antiquark pair as a function of distance for different temperatures. A value of the potential decreases with the temperature [4]. . . . .	7
1.5	A number of degrees of freedom as a function of a temperature [7]. . . . .	7
1.6	Phase diagram coming from the Lattice QCD calculations [8]. . . . .	8
1.7	Left: stages of a heavy ion collision simulated in the UrQMD model. Right: schematic view of a heavy ion collision evolution [8]. . . . .	9
1.8	Overlapping region which is created in heavy ion collisions has an almond shape. Visible x-z plane is a <i>reaction plane</i> . The x-y plane is a <i>transverse plane</i> . The z is a direction of the beam [11]. . . . .	11
1.9	Cross-section of a heavy ion collision in a transverse plane. The $b$ parameter is an <i>impact parameter</i> - a distance between centers of nuclei during a collision. An impact parameter is related with the centrality of a collision and a volume of the quark-gluon plasma [12]. . . . .	12
1.10	<i>Lower:</i> The elliptic flow $v_2$ follows the hydrodynamical predictions for an ideal fluid perfectly. Note that > 99% of all final hadrons have $p_T < 1.5 \text{ GeV}/c$ . <i>Upper left:</i> The $v_2$ plotted versus transverse kinetic energy $KE_T = m_T - m_0 = \sqrt{p_T^2 + m_0^2} - m_0$ . The $v_2$ follows different universal curves for mesons and baryons. <i>Upper right:</i> When scaled by the number of valence quarks, the $v_2$ follows the same universal curve for all hadrons and for all values of scaled transverse kinetic energy [13]. . . . .	13
1.11	Invariant yield of particles versus transverse mass $m_T = \sqrt{p_T^2 + m_0^2}$ for $\pi^\pm$ , $K^\pm$ , $p$ and $\bar{p}$ at mid-rapidity for p+p collisions (bottom) and Au+Au events from 70-80% (second bottom) to 0-5% (top) centrality [14]. . . . .	14

1.12 Thermal photons spectra for the central Au+Au collisions at $\sqrt{s_{NN}} = 200$ GeV computed within different hydrodynamical models compared with the pQCD calculations (solid line) and experimental data from PHENIX (black dots) [15]. . . . .	15
1.13 Left: Invariant mass spectrum of $e^+e^-$ pairs in Pb+Au collisions at 158A GeV compared to the sum coming from the hadron decays predictions. Right: The expectations coming from model calculations which assume a drop of the $\rho$ mass (blue) or a spread of the $\rho$ width in the medium (red) [16]. . . . .	16
1.14 Azimuthal angle difference $\Delta\phi$ distributions for different colliding systems at $\sqrt{s_{NN}} = 200$ GeV. Transverse momentum cut: $p_T > 2$ GeV. For the Au+Au collisions the away-side jet is missing [17]. . .	17
2.1 The cascade decay in the single freeze-out model. An unstable resonance $x_N$ is formed at the freeze-out hypersurface and travels for the time $\tau_N$ depending on its lifetime and decays. If the products are also resonances ( $x_{N-1}, x_2$ ) they decay further until the stable particles are formed ( $x_1$ ) [18]. . . . .	24
3.1 Bertsch-Pratt directions naming convention used in heavy ion collision. . . . .	26
3.2 The pair wave function is a superposition of all possible states. In case of particle interferometry it includes two cases: particles with momenta $p_1, p_2$ registered by detectors $A, B$ and $p_1, p_2$ registered by $B, A$ respectively. . . . .	27
3.3 A three-dimensional Gaussian source function with different widths was transformed into one-dimensional function. To illustrate deformations, one-dimensional Gaussian distribution was fitted. . . . .	30
3.4 Correlation function width dependence on the total pair momentum. Pion pairs with a large total momentum have a wider correlation (smaller apparent source) [28]. . . . .	34
4.1 Spherical harmonics coefficients of the two-pion correlation function. From the top left: $\Re C_0^0$ , $\Re C_2^0$ and $\Re C_2^2$ . Only selected centrality bins are presented for increased readability. . . . .	37
4.2 Spherical harmonics coefficients of the two-kaon correlation function. From the top left: $\Re C_0^0$ , $\Re C_2^0$ and $\Re C_2^2$ . Only selected centrality bins are presented for increased readability. The $\Re C_2^2$ is noisy, but one can still notice that it differs from zero and is becoming negative. . . . .	38

4.3 Spherical harmonics coefficients of the two-proton correlation function. From the top left: $\Re C_0^0$ , $\Re C_2^0$ and $\Re C_2^2$ . Only selected centrality bins are presented for increased readability. The $\Re C_2^0$ and $\Re C_2^2$ are noisy, but one can still notice, that they differ from zero and are becoming positive. . . . .	39
4.4 One-dimensional correlation function for pions (top left), kaons (top right) and protons (bottom) for different centralities. . . . .	40
4.5 One-dimensional correlation functions for pions, kaons and protons in the same centrality bin and different $k_T$ ranges. The plot was zoomed in to the region which illustrates the $k_T$ dependence in the best way. Only selected calculated ranges are presented for a better readability. . . . .	41
4.6 One-dimensional proton-proton correlation function. The red line represents analytical formula fit. . . . .	42
4.7 Femtoscopic radii in LCMS coming from two-pion correlation functions for all centrality bins as a function of $m_T$ . The dashed lines are power-law fits. The most central collisions (0-5%) are compared to the results from ALICE [31]. The two datasets are shifted to the right for a better visibility [30]. . . . .	43
4.8 Femtoscopic radii extracted from two-kaon correlation functions for different centrality bins as a function of $m_T$ . [30]. . . . .	44
4.9 Femtoscopic radii extracted from two-proton correlation functions for different centrality bins as a function of $m_T$ . [30]. . . . .	45
4.10 The results from the calculations for pions, kaons and protons for the three centralities presented on the same plot. One can notice that radii for particular centralities and different particle types follow the common power-law scaling. [30]. . . . .	46
4.11 Top left: one-dimensional radius for pions, kaons and protons calculated in PRF. Top right: the $R_{inv}$ scaled by the proposed factor. Bottom: averaged one-dimensional radius in LCMS for pions, kaons and protons. Only three centrality bins are shown for a better readability [30]. . . . .	47

Wydział Fizyki  
Politechniki Warszawskiej

Warszawa, dnia .....

## OŚWIADCZENIE

Ja, niżej podpisany:

Mateusz Gałażyn, 227143

student Wydziału Fizyki Politechniki Warszawskiej, świadomy/a odpowiedzialności prawnej oświadczam, że przedłożoną do obrony pracę dyplomową inżynierską/magisterską pt.:

*Calculation of predictions for non-identical particle correlations in heavy ions collisions at LHC energies from hydrodynamics-inspired models*

wykonałem samodzielnie pod kierunkiem dr hab.inż. Adama Kisiela, prof. PW

Jednocześnie oświadczam, że ww. praca:

- nie narusza praw autorskich w rozumieniu ustawy z dnia 4 lutego 1994 o prawie autorskim i prawach pokrewnych, oraz dóbr osobistych chronionych prawem cywilnym,
- nie zawiera danych i informacji uzyskanych w sposób niezgodny z obowiązującymi przepisami,
- nie była wcześniej przedmiotem procedur związanych z uzyskaniem dyplomu lub tytułu zawodowego w wyższej uczelni.

Oświadczam także, że treść pracy zapisanej na przekazanym nośniku elektronicznym jest zgodna z treścią zawartą w wydrukowanej wersji niniejszej pracy dyplomowej.

.....  
(podpis studenta)